Automation in Construction 177 (2025) 106371

Contents lists available at ScienceDirect

Automation in Construction

journal homepage: www.elsevier.com/locate/autcon

Uncertainty propagation in satellite InSAR data analysis for structural health monitoring

Pier Francesco Giordano [a,*], Antonios Kamariotis [b], Giorgia Giardina [c], Eleni Chatzi [b], Maria Pina Limongelli [a]

[a] Department of Architecture, Built Environment and Construction engineering, Politecnico di Milano, Piazza Leonardo da Vinci 32, 20133 Milan, Italy
[b] Department of Civil, Environmental and Geomatic Engineering, ETH Zürich, 8093 Zürich, Switzerland
[c] Department of Geoscience and Engineering, Delft University of Technology, Stevinweg 1, 2628 CN Delft, the Netherlands

ARTICLE INFO

Keywords:
Synthetic aperture radar interferometry
Displacement measurement
Satellite-based monitoring
Error propagation theory
Uncertainty
Grid subsampling
Structural health monitoring
COSMO-SkyMed
Civil structures

ABSTRACT

Structural Health Monitoring (SHM) supports the management of the integrity and functionality of critical infrastructure like bridges. Interferometric Synthetic Aperture Radar (InSAR) offers a scalable, non-intrusive alternative to conventional methods, ideal for large-scale and automated monitoring. However, spatial and temporal resampling, commonly used to reconstruct structural displacements from InSAR data, introduces uncertainty into final estimates. This paper presents a framework to quantify and reduce this uncertainty. A case study of a bridge in Rome, Italy, demonstrates that uncertainty metrics can effectively guide improvements in Persistent Scatterer (PS) clustering and grid configuration. Specifically, removing off-bridge PSs from a single grid cell reduced displacement uncertainty by 45 %, while replacing a fixed grid with a tailored layout for the entire bridge resulted in a 12 % average reduction in uncertainty. These findings provide valuable guidance for optimising InSAR data processing in SHM and underscore the critical role of PS clustering in improving measurement precision.

1. Introduction

Traditional Structural Health Monitoring (SHM) systems deliver continuous, real-time monitoring of civil structures and infrastructure through dedicated sensing setups, which include sensors and corresponding wired or tethered acquisition systems. These systems extract damage-sensitive features from physical measurements, offering insights into structural health over time [1–3]. Typically, this approach requires on-site sensor installation and maintenance, which can be labour-intensive and may not be feasible in all situations.

In recent years, the growing availability of Synthetic Aperture Radar (SAR) data, along with the enhanced resolution of SAR sensors, the reduced revisit time of SAR satellites and improvements in Synthetic Aperture Radar Interferometry (InSAR) methods [4,5], have significantly advanced the field of satellite-based remote monitoring of human-made structures [6,7]. This includes bridges [8,9], buildings [10,11], dams [12,13], as well as extensive linear infrastructures such as tunnels [14,15] and railways [16,17]. InSAR typically yields displacement time series at Persistent Scatterers (PSs), which are stable radar targets consistently detectable across multiple satellite acquisitions. Satellite-based InSAR offers a complementary approach to SHM by utilising remote sensing technology, thus avoiding the challenges of on-site sensor deployment.

Compared to traditional in-situ displacement measurement methods involving inclinometers, extensometers, and Global Navigation Satellite System (GNSS) receivers, InSAR techniques offer several advantages. A primary benefit is that they do not necessitate in-situ deployment of sensors, thereby avoiding the challenges associated with their installation and maintenance. Moreover, they allow for studying the past behaviour of structural systems, facilitating retroactive analysis of structural anomalies and collapse [18–20]. Additionally, they enable the investigation of large areas and data collection under any operational and environmental conditions. Nevertheless, manually extracting InSAR-derived displacement data from individual structures on a regional scale can be highly time-consuming and, therefore, impractical. Critical to the actionable application of these schemes is the development of efficient, automated procedures for structural monitoring based on InSAR data. Macchiarulo et al. [21] introduced a fully automated

* Corresponding author.
E-mail address: pierfrancesco.giordano@polimi.it (P.F. Giordano).

https://doi.org/10.1016/j.autcon.2025.106371
Received 21 October 2024; Received in revised form 20 June 2025; Accepted 23 June 2025
Available online 1 July 2025

methodology that combines InSAR data with GIS-based analysis to identify vulnerable infrastructure assets and critical sections along linear systems such as highways. Their approach processes large volumes of PS displacement time series alongside road network databases, enabling the automatic extraction of displacement data across extensive networks. It also includes localised analyses to identify abnormal differential movements within specific infrastructure sections. Nettis et al. [22] focused on bridges, proposing a portfolio-scale methodology for assessing structural displacements based on InSAR data. They utilise a completely automated geoprocessing chain composed of sequential algorithms that can be implemented within user-friendly GIS software packages. Each bridge is assigned a priority class that reflects the urgency for refined structural assessment and monitoring. Miano et al. [23] further advanced the field by presenting a large-scale automated analysis procedure aimed at preliminary evaluations of bridge health conditions within road networks. Their methodology also incorporates a bridge classification system, which aids in prioritising bridges within the network and ultimately assists infrastructure managers in allocating technical and financial resources over time.

Despite its numerous advantages, the application of InSAR techniques in structural monitoring presents challenges, particularly associated with the reconstruction of structural displacements [7]. Displacements are provided as one-dimensional data along the Line Of Sight (LOS) direction, which is the line connecting the satellite to the ground target. Also, the magnitude of measurable deformation along the LOS direction depends on the angle between the LOS and the direction of the target's displacement. Displacements parallel to the LOS can be measured with precision, whereas displacements perpendicular to the LOS would result in zero measured displacement, potentially leading to the oversight of significant deformations. Furthermore, due to the low incidence angle of SAR look directions, InSAR exhibits primary sensitivity to vertical displacements and may overlook north-south components [24].

The common approach to reconstructing structural displacements involves combining ascending and descending datasets acquired over the same area and spanning the same time window from the same constellation of satellites, as detailed in Section 2.2. More complex approaches that integrate data from different satellites have also been proposed [18]. Unfortunately, combining data from different orbits presents significant challenges. These include the non-homogeneous spatial distribution of PSs and the unlikely availability of LOS deformation measurements for the same point from ascending and descending orbits, typically only possible when artificial reflectors are installed [25]. Additionally, data from the ascending and the descending orbits are normally acquired at different time intervals, with the time gap potentially spanning several days. Hence, temporal and spatial resampling algorithms are generally employed to obtain consistent datasets [26,27]. Temporal resampling is typically performed using simple linear interpolation [10]. On the other hand, spatial resampling algorithms create spatially referenced points with LOS deformation data from different orbits, facilitating data combination. They include spatial interpolation, nearest neighbour, and grid subsampling.

Interpolation techniques for processing InSAR data can be deterministic, like Inverse Distance Weighted (IDW) [28,29], or probabilistic nature, such as Kriging techniques [30,31]. Interpolation methods have the advantage of delivering continuous maps of displacement measurements, although accounting for the three-dimensional nature of InSAR data remains non-trivial. The nearest neighbour method [26,32] combines PSs from different orbits based on their vicinity and uses a search distance algorithm, preserving the spatial information associated with PSs. Grid subsampling is a straightforward technique that involves dividing the area of interest into cells of a chosen size and averaging the displacements of the PSs within each cell [33,34]. In the case of civil structures, such as bridges, it might involve partitioning the structures into polygonal areas, where PSs are clustered under the assumption that they present similar behaviour [9,35]. Grid subsampling offers a method that is highly suited for automation. Exploiting this tool, Macchiarulo et al. [21] automatically divided roadway networks into rectangular regions of equal area, with the rectangles rotated to align with their respective road segments, allowing the grid to adapt to the shape of the infrastructure. Similarly, Nettis et al. [22] employed an automated procedure utilising a clustering approach to calculate the deformation velocities for various longitudinal sections of bridges. The European Ground Motion Service (EGMS) [36] provides vertical and east-west displacements on a fixed 100 by 100 m grid with square cells. However, it remains unclear how to optimally select the cell location, shape, number, and dimension.

Temporal and spatial resampling algorithms involve various operations that inevitably introduce uncertainty into the reconstructed displacement data, which must be considered when interpreting the results. This challenge becomes even more critical when large-scale automated procedures are implemented with limited or no human oversight. Despite its importance, this topic has not received the attention it deserves in the existing literature.

Few studies have addressed the uncertainty quantification of structural displacement reconstructed using LOS InSAR data. Assessing the uncertainty in InSAR-derived displacements is not only crucial for interpreting results but also essential for conducting structural reliability analyses [37]. Farneti et al. [9] introduced a method to quantify the error in reconstructed structural displacements by accounting for the precision of LOS measurements, the orientation of the bridge, and the assumed deformation plane. Similarly, Bassoli et al. [38] developed a framework for reconstructing the rigid motion of a building from LOS displacements, offering an analytical approach to quantify the uncertainties affecting the estimated motion parameters. However, to the best of the authors' knowledge, the error introduced in reconstructed displacements due to temporal and spatial resampling has yet to be investigated. This aspect has received less attention in the literature compared to raw measurement uncertainties, and our work aims to fill this gap [39–41].

In summary, two key gaps motivate this study. First, while spatial and temporal resampling are standard steps in InSAR data processing, the uncertainty they introduce into reconstructed displacements is typically not quantified. Second, there is no established methodology for defining spatial discretisation in the context of grid subsampling. This paper addresses these research gaps through the following contributions:

- It introduces a framework based on error propagation theory for quantifying the uncertainty introduced by spatial and temporal resampling.
- It offers a comparative analysis of different grid configurations, including regular and structure-aligned layouts, highlighting how spatial subdivision influences measurement precision.
- It demonstrates that elevated displacement variability within a given area may indicate inconsistent PS clustering, suggesting further analysis.
- It proposes dedicated uncertainty metrics to support the identification of optimal grid configurations.

We apply the proposed framework to the Palatino Bridge crossing the Tiber River in Rome, Italy. The bridge, approximately 155 m long, consists of a continuous metal truss resting on masonry supports and exhibits significant thermal deformations. The analysis of satellite data was conducted by CNR-IREA (the Institute for Electromagnetic Sensing of the Environment, part of the Italian National Research Council) as part of the ReLUIS Project "Structural Health Monitoring and Satellite Data" WP6–2019-21, which led to the definition of the first "Guidelines for the use of satellite interferometric data for interpreting the behaviour of structures" [42]. Specifically, the displacements were obtained using the COSMO-SkyMed (CSK) dataset acquired from July 2011 to March 2019 in StripMAP HIMAGE mode. The dataset was processed using the

"Parallel SBAS Interferometry Chain" technique [43,44].

Following this introduction, Section 2 provides background on InSAR monitoring, including the fundamental principles of the technique (2.1), typical processing workflows (2.2), and the concepts of grid subsampling (2.3) and temporal resampling (2.4). Section 3 introduces the proposed method, detailing the approach to uncertainty quantification (3.1) and the strategy for grid optimisation (3.2). Section 4 demonstrates the application of the method through a real-world case study, including a description of the monitored structure (4.1), the InSAR dataset used (4.2), and the analysis results (4.3). The Discussion is presented in Section 5, focusing on the performance evaluation, the comparisons with the state-of-the-art, and the method's limitations, as well as future steps toward automation. Section 6 concludes the paper. Additional material related to the mathematical formulation of error propagation is provided in the Appendix.

2. Background on InSAR

This section introduces the key concepts and workflows for understanding InSAR-based structural monitoring. It begins by explaining how SAR sensors emit microwave pulses and record backscattered signals, which are processed into radar images containing both amplitude and phase components. These images are then used to generate interferograms and derive displacement time series. We also cover spatial grid subsampling, which aggregates displacement measurements from PSs into defined cells, and temporal resampling, which aligns time series across different acquisition dates. These topics lay the technical foundation for the later examination of how uncertainty propagates through these processing steps and for exploring optimisation strategies.

2.1. InSAR principles

InSAR is based on data acquired by SAR systems—active sensors that operate in the microwave band, using wavelengths from approximately 1 mm to 100 cm [45]. SAR systems transmit electromagnetic pulses toward the Earth's surface and record the backscattered signals to generate high-resolution radar images [46]. Each image consists of a matrix of complex values, where the amplitude reflects the strength of the returned signal and the phase corresponds to the signal's round-trip travel distance. These characteristics are influenced by surface properties such as roughness, geometry, and material composition, making SAR particularly well-suited for deformation monitoring under various environmental conditions. Satellites equipped with SAR sensors, in general, follow near-polar orbits, acquiring imagery either in a south-to-north (ascending) or north-to-south (descending) direction. The imaging is done with a side-looking geometry shown in Fig. 1, and the LOS usually forms an incidence angle between 20° and 50° from vertical. SAR missions currently operate in different wavelength bands—L-, C-, and X-band—each suited to different monitoring scales and surface conditions. Shorter wavelengths (e.g., X-band) enable higher spatial resolution, whereas longer wavelengths (e.g., L-band) better penetrate vegetation and provide more stable phase coherence.

InSAR techniques exploit the phase difference between two SAR images acquired over the same area at different times to detect ground deformation [47]. The underlying principle is that the phase of a radar signal is directly related to the distance between the satellite and the ground target. When two images are acquired at times t_0 and t_1, any change in this distance due to surface movement produces a measurable interferometric phase difference $\Delta\Phi$, which can be expressed as

$$\Delta\Phi = \frac{4\pi}{\lambda}\Delta r \tag{1}$$

where λ is the radar wavelength and Δr is the change in the range distance between the sensor and the ground target. The resulting interferogram contains phase information that reflects any change in distance between the satellite and the target, as shown in Fig. 2. This phase variation is proportional to deformation but also includes unwanted contributions from topography, Earth curvature, atmospheric conditions, and noise. These must be carefully removed or minimised to retrieve accurate displacement information. The remaining deformation phase can then be converted to LOS displacement.

Early applications were based on Differential InSAR (DInSAR), which compares just two SAR acquisitions [48]. While effective for capturing sudden or large displacements, DInSAR suffers from sensitivity to temporal decorrelation, geometric baseline variations, and atmospheric disturbances, particularly in non-urban or vegetated regions. To overcome these limitations, Multi-Temporal InSAR (MT-InSAR) techniques were developed in the late 1990s. MT-InSAR methods process long sequences of SAR images to improve phase stability and measurement reliability. Two widely used MT-InSAR techniques are Permanent

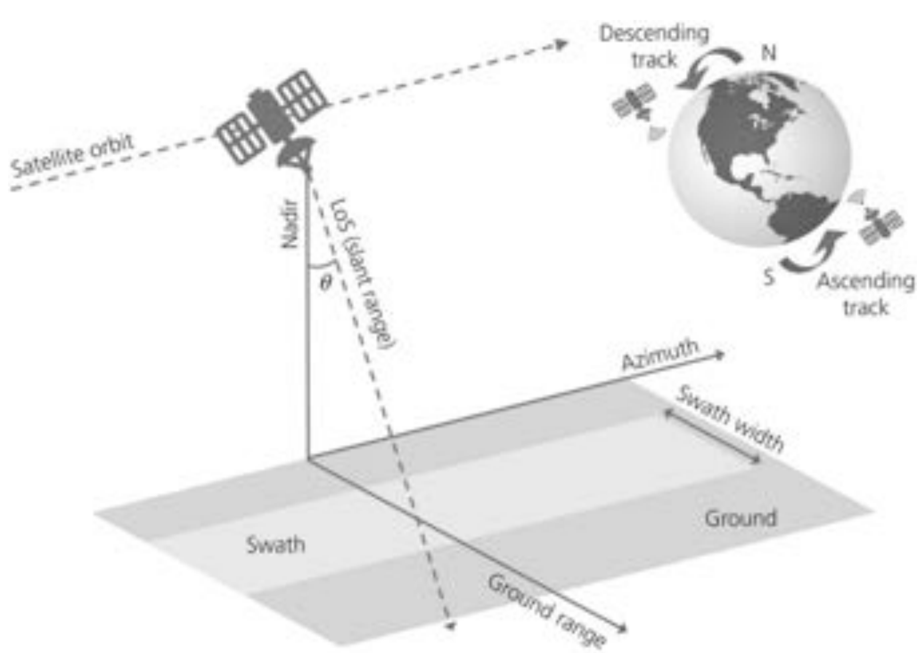

Fig. 1. Schematic representation of the side-looking geometry of SAR satellites (from [7]).

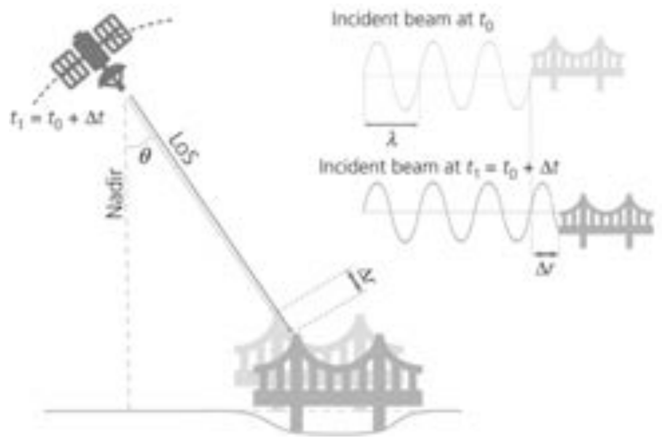

Fig. 2. Basic concept of InSAR: measurement of ground deformation by comparing the phase information (from [7]).

Scatterer Interferometry (PSI) [49] and Small Baseline Subset (SBAS) [5]. These approaches focus on identifying and analysing PSs—points on the ground that reflect radar signals consistently over time, such as buildings, bridges, or rock outcrops.

PSs are geolocated in 3D space and serve as natural geodetic markers. Displacement time series and mean velocities can be derived with millimetre-scale precision, referenced to a stable point within the scene. The results are typically provided as a geospatial dataset containing PS coordinates, elevation, temporal coherence, and deformation measurements. These dense PS networks offer a measurement capability comparable to GNSS arrays but without the need for physical instrumentation on the ground.

The advent of second-generation SAR missions, such as TerraSAR-X, COSMO-SkyMed, and Sentinel-1, has significantly enhanced MT-InSAR performance by delivering higher spatial resolution and shorter revisit intervals [50]. More recently, commercial constellations like ICEYE [51] and Capella [52] are enabling near-real-time monitoring with sub-metre resolution and daily or even hourly observations.

2.2. InSAR data processing

In principle, a comprehensive reconstruction of the three-dimensional deformation field can be achieved by combining LOS measurements along at least three non-parallel directions or integrating in-situ measurements. This approach involves the independent processing of different datasets covering the same location acquired within the same period to retrieve LOS deformation measurements for each viewing geometry. However, generally, only data from the ascending and descending orbits are available.

Using the properties of the scalar product between vectors, the displacement from the ascending $d_{LOS,A}$ and the descending $d_{LOS,D}$ orbits can be expressed as a function of the components of the displacements along the east-west, d_E, north-south, d_N, and vertical, d_U, directions according to the following Eqs. [10]:

$$\begin{cases} d_{LOS,A} = d_E \cdot c_{E,A} + d_N \cdot c_{N,A} + d_U \cdot c_{U,A} \\ d_{LOS,D} = d_E \cdot c_{E,D} + d_N \cdot c_{N,D} + d_U \cdot c_{U,D} \end{cases} \tag{2}$$

where $c_{E,A/D}$, $c_{N,A/D}$, $c_{U,A/D}$ represent the direction cosines corresponding to the angles $\alpha_{E,A/D}$, $\alpha_{N,A/D}$, $\alpha_{U,A/D}$, defined between the east-west (E), north-south (N), and vertical (U) directions and the LOS direction with unit vector $\hat{\mathbf{v}}_{LOS_{A/D}}$, respectively; the subfix A relates to the ascending orbit while the subfix D relates to the descending one. To better clarify the variables used in the eqs. (2), Fig. 3 represents ascending (Fig. 3a) and descending (Fig. 3b) geometries as well as the displacement vector and its components (Fig. 3c).

Usually, the known data includes direction cosines and LOS displacements, while the real displacement components are unknown. This results in a system of two equations with three unknowns, which is indeterminate. A common approach to solving the system of eqs. (2) is to assume that the displacements occur on a plane. Farneti et al. [9] propose a method for processing InSAR data that enables the two-dimensional reconstruction of bridge displacements over time. They decompose the bridge displacements into a reference system composed of longitudinal, transverse, and vertical directions, where the longitudinal direction follows the length of the bridge. The reconstruction of the bridge's behaviour is achieved by assuming that one of these components is null, which is equivalent to knowing the plane in which the displacement vector lies.

Here, in reconstructing structural displacements, the displacement in the N direction is constrained to zero, under the assumption that displacement occurs within the E-U plane [7,27]. This assumption, while not physically based, arises from the sensor's inability to detect displacements along the N-S direction [24]. As a result, the system of equations is simplified, allowing for the determination of the remaining displacement components in the E and U directions:

$$\begin{cases} d_{LOS,A} = d_E \cdot c_{E,A} + d_U \cdot c_{U,A} \\ d_{LOS,D} = d_E \cdot c_{E,D} + d_U \cdot c_{U,D} \end{cases} \tag{3}$$

By solving the system of equations, the U- and E-direction displacements are computed as follows:

$$\begin{cases} d_E = a_E \cdot d_{LOS,D} - b_E \cdot d_{LOS,A} \\ d_U = a_U \cdot d_{LOS,A} - b_U \cdot d_{LOS,D} \end{cases} \tag{4}$$

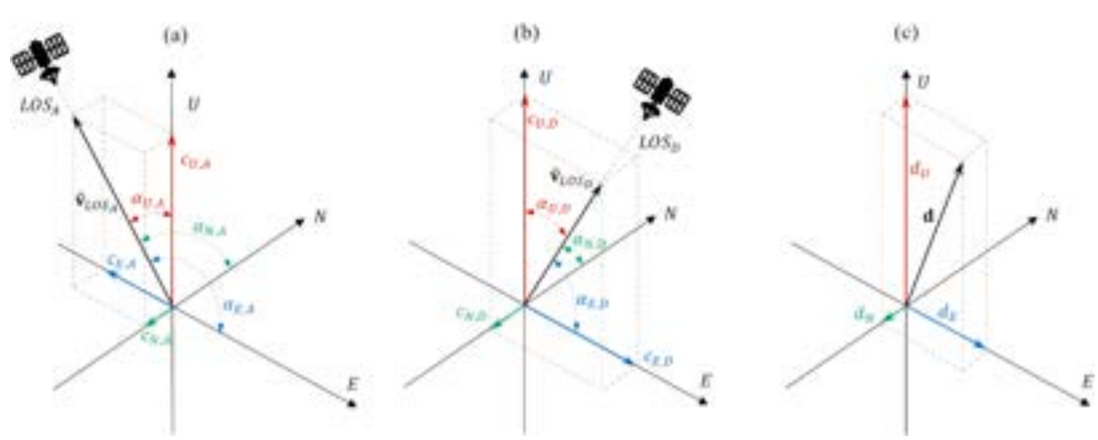

Fig. 3. Schematic representation of the (a) ascending and (b) descending geometries with unit vectors ($\hat{\mathbf{v}}_{LOS_{A/D}}$), angles between the LOS and the E, N and U directions ($\alpha_{E,A/D}$, $\alpha_{N,A/D}$, $\alpha_{U,A/D}$), and direction cosines ($c_{E,A/D}$, $c_{N,A/D}$, $c_{U,A/D}$); (c) displacement vector $\mathbf{d}$ and its components (d_E, d_N, d_U).

where

$$\begin{cases} a_E = \dfrac{c_{U,A}}{c_{U,A} \cdot c_{E,D} - c_{U,D} \cdot c_{E,A}}; b_E = \dfrac{c_{U,D}}{c_{U,A} \cdot c_{E,D} - c_{U,D} \cdot c_{E,A}} \\ a_U = \dfrac{c_{E,D}}{c_{U,A} \cdot c_{E,D} - c_{U,D} \cdot c_{E,A}}; b_U = \dfrac{c_{E,A}}{c_{U,A} \cdot c_{E,D} - c_{U,D} \cdot c_{E,A}} \end{cases} \tag{5}$$

Due to the distance between the satellites and the Earth's surface, the direction cosines, and consequently the coefficients in eqs. (5), can be assumed to remain fixed when investigating a single structure, i.e., these do not vary over time. The error in the estimation of d_E and d_U using eqs. (4) is small if the terms $c_{N,A/D}$ or d_N approach zero.

When only data from a single orbit are available, additional assumptions about structural behaviour are necessary. A common approach involves assuming null horizontal displacements ($d_E = 0$ and $d_N = 0$), see for instance [14,53]. Huang et al. [54], while examining a railway bridge, assume that the LOS deformation is exclusively due to longitudinal displacement along the bridge and propose a simplified method for converting LOS displacements into longitudinal displacement. Another approach [55], also developed for bridges, incorporates knowledge of structural behaviour by accounting for longitudinal displacements caused by temperature variations while assuming null displacements in the transverse direction. While these methods can work effectively in certain cases, their applicability should be carefully evaluated against the particular properties of the bridge in question.

In addition to the assumptions about structural behaviour that result in setting one or more displacement components to zero, merging datasets from different orbits introduces further complexities related to the spatial and temporal resampling of displacement data. In fact, in practice, the system of eqs. (4) cannot be directly applied. This is due not only to the non-uniform spatial distribution of PSs from the ascending and descending datasets but also to the fact that SAR satellites with opposite orbits pass over the same area with a temporal offset of a few days between observations. In the following sections, we address these issues by adopting two common approaches: grid subsampling and linear temporal interpolation.

2.3. Grid subsampling

To address the non-uniform distribution of PSs in ascending and descending datasets, a widely adopted approach involves creating a grid that is independent of viewing geometry, where - ideally - each area contains PSs from both the ascending and the descending orbit. Fig. 4 represents a typical situation, where PSs from opposite orbits are organised into a grid with square areas. After defining the grid, each cell's centre is assigned a deformation value, which is the average of the deformation values of the PSs within that cell. This process creates synthetic PSs at the centre of each cell, providing a more uniform spatial representation of deformation measurements.

If the grid size is too small, there may not be enough measurement points within each cell. For instance, as shown in Fig. 4, data from the descending orbit are present in cell (e,b), but data from the ascending orbit are not present in the same cell, meaning that vertical and horizontal displacements cannot be reconstructed in that area using eqs. (4). In general, the grid size used for analysing SAR data should not be smaller than the resolution of the SAR sensor. On the other hand, if the grid size is too large, displacements of PSs belonging to different structural elements might be averaged, providing meaningless results. Therefore, the selection of an appropriate grid is crucial for obtaining precise and useful displacement measurements.

Eqs. (4) can be rewritten by considering the displacements of the n-th area, $n = 1, \ldots, N$, measured at time t, as shown below:

$$\begin{cases} d^t_{E,n} = a_E \cdot d^t_{LOS,D,n} - b_E \cdot d^t_{LOS,A,n} \\ d^t_{U,n} = a_U \cdot d^t_{LOS,A,n} - b_U \cdot d^t_{LOS,D,n} \end{cases} \tag{6}$$

At each time t, the displacements associated with each PS within a given n-th area are interpreted as repeated, independent direct measurements taken under the same conditions of the quantity being measured, i.e., the displacement along the LOS of a structural element or portion of the structure under investigation. From these measurements, we can calculate the sample mean and the standard deviation.

For the n-th area, the sample mean displacements at time t from the two orbits are determined using the following equations:

$$d^t_{LOS,A,n} = \frac{1}{M} \sum_{m=1}^{M} d^t_{LOS,A,n,m} \tag{7}$$

$$d^t_{LOS,D,n} = \frac{1}{L} \sum_{l=1}^{L} d^t_{LOS,D,n,l} \tag{8}$$

where $d^t_{LOS,A,n,m}$ is the displacement of the m-th PSs ($m = 1, \ldots, M$) from

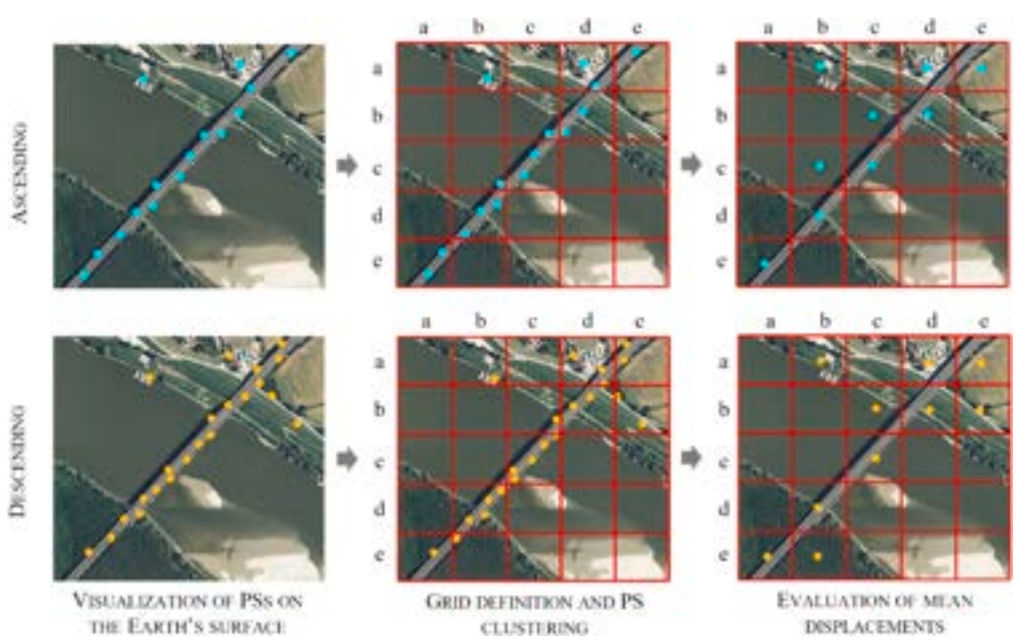

Fig. 4. Grid definition and PS clustering.

the ascending orbit, $d^t_{LOS,D,n,l}$ is the displacement of the l-th PSs ($l = 1,\ldots, L$) from the descending orbit, M and L are the total number of PSs in the n-th area for the ascending and descending orbit, respectively. In general, M and L are different for the same area. The corresponding sample standard deviations read:

$$\sigma_{d^t_{LOS,A,n}} = \sqrt{\frac{1}{M-1}\sum_{m=1}^{M}\left(d^t_{LOS,A,n} - d^t_{LOS,A,n,m}\right)^2} \text{ for } M \geq 2 \tag{9}$$

$$\sigma_{d^t_{LOS,D,n}} = \sqrt{\frac{1}{L-1}\sum_{l=1}^{L}\left(d^t_{LOS,D,n} - d^t_{LOS,D,n,l}\right)^2} \text{ for } L \geq 2 \tag{10}$$

The standard deviations can change over time according to the behaviour of the displacement time series of individual PSs. Also, it is important to note that the LOS displacement time series at each PS are provided as values relative to an initial reference displacement, which is not known in absolute terms. Often, this initial displacement is set to zero. By applying an offset to all values in the time series, different normalisations can be achieved, such as time series with a null mean displacement. In turn, the standard deviations depend on the initial normalisation applied to express the LOS displacement time series.

Another quantity of interest is the standard deviation of the sample means of the LOS displacements, which decreases as the number of PSs inside the n-th area increases:

$$\sigma_{\mu_{d^t_{LOS,A,n}}} = \sqrt{\frac{1}{M(M-1)}\sum_{m=1}^{M}\left(d^t_{LOS,A,n} - d^t_{LOS,A,n,m}\right)^2} \text{ for } M \geq 2 \tag{11}$$

$$\sigma_{\mu_{d^t_{LOS,D,n}}} = \sqrt{\frac{1}{L(L-1)}\sum_{l=1}^{L}\left(d^t_{LOS,D,n} - d^t_{LOS,D,n,l}\right)^2} \text{ for } L \geq 2 \tag{12}$$

Given the same standard deviation, areas with a higher number of PSs will feature a lower standard deviation of the sample mean. However, the square root of the number of PSs in the denominator indicates that reducing the uncertainty associated with the sample mean requires an increasingly large number of PSs.

2.4. Temporal resampling

Temporal resampling involves oversampling the original signal, enabling adjustments to the desired sampling frequency for each dataset. In this study, we focus on linear interpolation, as this technique is widely used in practice. Let us assume that $d^{t-1}_{LOS,A/D,n}$ and $d^{t+1}_{LOS,A/D,n}$ are two consecutive measurements of LOS displacements, either from the ascending or the descending orbit, acquired at discrete time t_{-1} and time t_{+1}, respectively. The interpolated value $\widehat{d}^t_{LOS,A/D,n}$ at time t, where $t_{-1} < t < t_{+1}$, is obtained using the linear interpolation formula:

$$\widehat{d}^t_{LOS,A/D,n} = d^{t_{-1}}_{LOS,A/D,n} + \left(d^{t_{+1}}_{LOS,A/D,n} - d^{t_{-1}}_{LOS,A/D,n}\right)\frac{t - t_{-1}}{t_{+1} - t_{-1}} \tag{13}$$

After some passages, the interpolated displacement can be written as follows:

$$\widehat{d}^t_{LOS,A/D,n} = c^t_1 \cdot d^{t_{-1}}_{LOS,A/D,n} + c^t_2 \cdot d^{t_{+1}}_{LOS,A/D,n} \tag{14}$$

where

$$\begin{cases} c^t_1 = \dfrac{t_{+1} - t}{t_{+1} - t_{-1}} \\ c^t_2 = \dfrac{t - t_{-1}}{t_{+1} - t_{-1}} \end{cases} \tag{15}$$

The coefficients c^t_1 and c^t_2 depend only on the times t, t_{-1} and t_{+1} and range between 0 and 1.

Two situations occur during the computation of displacements along the vertical and the E direction. The first situation is when the LOS displacement corresponding to the ascending orbit is available and the one corresponding to the descending orbit is interpolated, as represented in Fig. 5.

In this case, eqs. (6) are re-formulated as follows:

$$\begin{cases} d^t_{E,n} = a_E \cdot \widehat{d}^t_{LOS,D,n} - b_E \cdot d^t_{LOS,A,n} \\ d^t_{U,n} = a_U \cdot d^t_{LOS,A,n} - b_U \cdot \widehat{d}^t_{LOS,D,n} \end{cases} \tag{16}$$

After substituting eq. (14) in eqs. (16), we obtain:

$$\begin{cases} d^t_{E,n} = a_E \cdot c^t_1 \cdot d^{t_{-1}}_{LOS,D,n} + a_E \cdot c^t_2 \cdot d^{t_{+1}}_{LOS,D,n} - b_E \cdot d^t_{LOS,A,n} \\ d^t_{U,n} = a_U \cdot d^t_{LOS,A,n} - b_U \cdot c^t_1 \cdot d^{t_{-1}}_{LOS,D,n} - b_U \cdot c^t_2 \cdot d^{t_{+1}}_{LOS,D,n} \end{cases} \tag{17}$$

The system of eqs. (17) expresses the horizontal and vertical displacement of area n at time t as a linear function of known coefficients and measured LOS displacements.

The second situation is when the LOS displacement corresponding to the descending orbit is available and the one corresponding to the ascending orbit is interpolated, see Fig. 6.

In this situation, the system of eqs. (6) is re-formulated as follows:

$$\begin{cases} d^t_{E,n} = a_E \cdot d^t_{LOS,D,n} - b_E \cdot \widehat{d}^t_{LOS,A,n} \\ d^t_{U,n} = a_U \cdot \widehat{d}^t_{LOS,A,n} - b_U \cdot d^t_{LOS,D,n} \end{cases} \tag{18}$$

Substituting eq. (14) in eqs. (18), we obtain:

$$\begin{cases} d^t_{E,n} = a_E \cdot d^t_{LOS,D,n} - b_E \cdot c^t_1 \cdot d^{t_{-1}}_{LOS,A,n} - b_E \cdot c^t_2 \cdot d^{t_{+1}}_{LOS,A,n} \\ d^t_{U,n} = a_U \cdot c^t_1 \cdot d^{t_{-1}}_{LOS,A,n} + a_U \cdot c^t_2 \cdot d^{t_{+1}}_{LOS,A,n} - b_U \cdot d^t_{LOS,D,n} \end{cases} \tag{19}$$

Similarly to the system of eqs. (17), also eqs. (19) express the horizontal and the vertical displacement of area n at time t as a linear function of known coefficients and measured LOS displacements.

3. Proposed method

Following the introduction to InSAR-based monitoring and the relevant processing equations, covering how structural displacements are derived and resampled in space and time, this section presents our proposed framework for quantifying the resulting uncertainty. We first describe the theoretical foundation based on error propagation and introduce key metrics designed to capture uncertainty in displacement estimates. Next, we explore optimisation schemes for grid design that employ these uncertainty metrics to improve displacement results across the monitored area.

3.1. Uncertainty quantification

The inherent uncertainty in InSAR data is taken into account by treating displacement measurements within a given spatial region as repeated observations of the same underlying deformation process. By analysing the variability of these observations, we estimate the dispersion of displacement values, which reflects the contribution of measurement noise and residual atmospheric effects. This approach allows

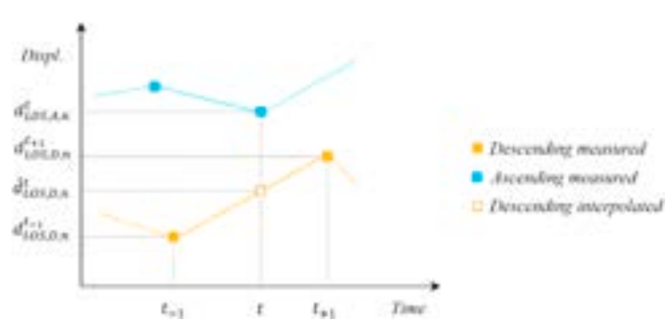

Fig. 5. Interpolation of descending data at ascending dataset acquisition times.

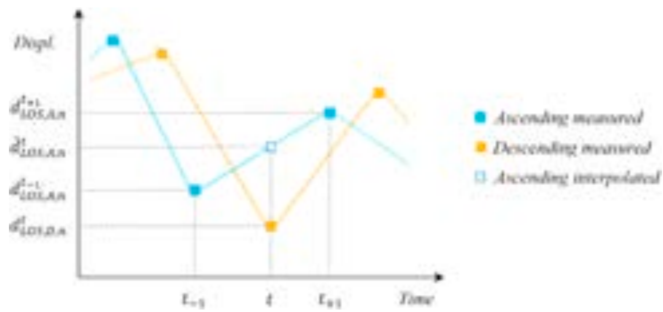

Fig. 6. Interpolation of ascending data at descending data acquisition times.

us to assess how resampling influences the precision of displacement estimates without requiring explicit modelling of individual error sources.

To quantify the uncertainty affecting the reconstructed horizontal and vertical displacements, we apply classic propagation error theory [56]. Consider a differentiable function $y = f(x_1, \ldots, x_k)$ of k measured random variables with means $\mu_{x_1}, \ldots, \mu_{x_k}$ and standard deviations $\sigma_{x_1}, \ldots, \sigma_{x_k}$. By repeating p direct measurements for each of the k variables, a distribution of y values is derived from the different realizations of these random variables. Under the assumptions that (1) the direct measurements are affected by sufficiently small errors to justify the linearization of the quantity y; and (2) there is no mutual influence between the measurements of the different quantities, meaning the directly measured quantities are independent, the expected value μ_y and the standard deviation σ_y of y are obtained as follows:

$$\mu_y = f\left(\mu_{x_1}, \ldots, \mu_{x_k}\right) \tag{20}$$

$$\sigma_y = \sqrt{\sum_{j=1}^{k} \left(\frac{\partial f}{\partial x_j}\right)^2 \sigma_{x_j}^2} \tag{21}$$

The derivations of these equations are provided in the Appendix. As for condition (1), in the previous section, we demonstrated that the reconstructed displacements in the U- and E- directions can be expressed as a linear combination of a set of coefficients and LOS displacements, as indicated in (17) and (19). The procedure described is exact when the quantity y is a linear combination of independent variables, expressed as $y = \pm a \cdot x_1 \pm b \cdot x_2 \pm \ldots$. In this case, eq. (21) simplifies to:

$$\sigma_y = \sqrt{a^2 \cdot \sigma_{x_1}^2 + b^2 \cdot \sigma_{x_2}^2 + \ldots} \tag{22}$$

This equation can then be used to determine the standard deviations of the reconstructed displacements, where σ_y becomes their standard deviation and the terms σ_{x_j} are the standard deviations of the LOS displacement calculated using eqs. (9) and (10), multiplied by known coefficients. Regarding condition (2), PSs inside a grid area are treated as independent measurements of displacement along the LOS.

Having established the theoretical framework, we can now define the standard deviation of the reconstructed displacements. When the LOS displacement for the ascending orbit is directly available, and the displacement for the descending orbit is interpolated, the standard deviations for $d_{E,n}^t$ and $d_{U,n}^t$, derived using eqs. (17), read:

$$\begin{cases} \sigma_{d_{E,n}^t} = \sqrt{a_E^2 \cdot c_1^{t\,2} \cdot \sigma^2_{d^{t-1}_{LOS,D,n}} + a_E^2 \cdot c_2{}^2 \cdot \sigma^2_{d^{t+1}_{LOS,D,n}} + b_E^2 \cdot \sigma^2_{d^t_{LOS,A,n}}} \\ \sigma_{d_{U,n}^t} = \sqrt{a_U^2 \cdot \sigma^2_{d^t_{LOS,A,n}} + b_U^2 \cdot c_1^{t\,2} \cdot \sigma^2_{d^{t-1}_{LOS,D,n}} + b_U^2 \cdot c_2{}^2 \cdot \sigma^2_{d^{t+1}_{LOS,D,n}}} \end{cases} \tag{23}$$

Conversely, when the LOS displacements for the descending orbit are directly available and the displacement for the ascending orbit is interpolated, $d_{E,n}^t$ and $d_{U,n}^t$ are calculated using eqs. (19), with their standard deviations determined as follows:

$$\begin{cases} \sigma_{d_{E,n}^t} = \sqrt{a_E^2 \cdot \sigma^2_{d^t_{LOS,D,n}} + b_E^2 \cdot c_1^{t\,2} \cdot \sigma^2_{d^{t-1}_{LOS,A,n}} + b_E^2 \cdot c_2^{t\,2} \cdot \sigma^2_{d^{t+1}_{LOS,A,n}}} \\ \sigma_{d_{U,n}^t} = \sqrt{a_U^2 \cdot c_1^{t\,2} \cdot \sigma^2_{d^{t-1}_{LOS,A,n}} + a_U^2 \cdot c_2^{t\,2} \cdot \sigma^2_{d^{t+1}_{LOS,A,n}} + b_U^2 \cdot \sigma^2_{d^t_{LOS,D,n}}} \end{cases} \tag{24}$$

3.2. Grid optimisation

A common challenge in InSAR data analysis is determining the optimal grid configuration. Decisions may also need to be made regarding the exclusion of certain PSs from the calculation of mean displacement for each area or the selection of the initial normalisation criterion for LOS displacement time histories. Filtering criteria for PSs can involve factors such as temporal coherence [57] or geometric considerations. For the initial normalisation of LOS displacements, the typical approach is to set the first displacement to zero, although alternative criteria - as discussed in the following sections - could also be applied. The uncertainty associated with displacement measurements can inform the selection of the optimal grid configuration for clustering PSs from opposite orbits, as well as the choice of which PSs to include in the analysis. Given a set of possible grid configurations, which may incorporate PS selection criteria, $\Omega = [C_1, C_2, \ldots]$, the metrics $\overline{\sigma}_{d_{E,C_i}}$ and $\overline{\sigma}_{d_{U,C_i}}$ are proposed to quantify the overall uncertainty associated with the vertical and longitudinal displacements, respectively, as follows:

$$\overline{\sigma}_{d_{U,C_i}} = \frac{1}{N_{C_i}} \sum_{n=1}^{N_{C_i}} \frac{1}{T} \sum_{t=1}^{T} \sigma_{d_{U,n}^t} = \frac{1}{N_{C_i}} \sum_{n=1}^{N_{C_i}} \overline{\sigma}_{d_{U,n}} \tag{25}$$

$$\overline{\sigma}_{d_{E,C_i}} = \frac{1}{N_{C_i}} \sum_{n=1}^{N_{C_i}} \frac{1}{T} \sum_{t=1}^{T} \sigma_{d_{E,n}^t} = \frac{1}{N_{C_i}} \sum_{n=1}^{N_{C_i}} \overline{\sigma}_{d_{E,n}} \tag{26}$$

where T is the total number of values in the displacement time histories, N_{C_i} is the number of areas corresponding to the configuration C_i, $\overline{\sigma}_{d_{E,n}}$ and $\overline{\sigma}_{d_{U,n}}$ represent the mean standard deviation of the displacements over the observation period in the n-th area.

The proposed metrics provide the mean standard deviation of displacements across different areas and over the entire observation period. These metrics can be used to quantify the uncertainty introduced by various processing choices and grid configurations. They enable direct comparison of factors such as grid geometric properties, filters applied to PSs (e.g., elevation-based filtering), and the initial normalisation methods used for LOS displacement time series. By evaluating these metrics across several grid configurations, it becomes possible to identify the best setup among several considered options that minimises uncertainty.

4. Demonstration of the proposed approach

In this section, we demonstrate the application of our uncertainty quantification framework to a real-world case study. First, we present the bridge under analysis and describe the available InSAR dataset. We then explore how different grid configurations and processing choices affect the results. Specifically, we begin with a regular grid for clustering PSs, then compare these results to those obtained with a tailored grid layout. We also investigate the impact of displacement normalisation on uncertainty metrics.

4.1. Case study

Spanning the Tiber River in Rome, Italy, the Palatino Bridge was constructed between 1886 and 1890 to replace the remnants of the ancient Roman arch stone bridge known as the “Broken Bridge” (Ponte Rotto). Fig. 7 illustrates this structure, which measures approximately 155 m in length and 20 m in width. Archival material [58] provides detailed historical and structural information on the Palatino Bridge,

Fig. 7. Palatino bridge: (a) Aerial view of the bridge (from Google Maps); (b) Focus on the piers; (c) Focus on the continuous beams.

including material properties and geometric specifications. The bridge is a continuous iron truss structure supported by six masonry supports: four piers and two abutments. These supports have foundations in the water, made of stone masonry, which extend to varying depths between 10 and 16 m below the riverbed. The piers are characterised by their substantial thickness, which is 5 m at the base and narrows to 3 m at the top. Internally, the abutments and piers comprise tuff masonry; externally, they are clad with travertine blocks. Granite blocks form the top of the piers, on which cast-iron plates are embedded, providing a base for the trusses.

The bridge's piers and abutments are oriented at different angles relative to the longitudinal axis of the deck. According to [58], the deck is anchored with fixed constraints to the second pier from west to east, whereas the other piers utilise cylindrical roller bearings to support the deck, allowing for controlled movement and accommodating thermal expansion. Additionally, the deck is connected to the abutments via two joints positioned at each end. The bridge experiences horizontal displacement primarily along its longitudinal axis due to seasonal thermal expansion, which closely aligns with the *E*-direction. Instead, movement in the N-direction is expected to be minimal. [35,59]

4.2. InSAR data

As introduced in the previous sections, the interferometric analysis of surface displacements in the Rome area was carried out using the SBAS-DInSAR technique, developed by IREA-CNR starting in 2001 and consolidated in the years that followed. Two CSK datasets were selected: the first consists of 129 ascending images acquired between March 2011 and March 2019, and the second of 107 descending images acquired between July 2011 and March 2019. From these datasets, a total of 392 ascending and 332 descending differential interferograms were generated. A maximum perpendicular baseline threshold of 1000 m was applied to avoid significant phase decorrelation, which can occur with larger baselines. The CSK constellation operates in the X-band, with a wavelength of approximately 3.1 cm, which offers high sensitivity to small surface displacements and is particularly suitable for monitoring urban infrastructure. The differential interferograms were generated using a Digital Elevation Model (DEM) derived from the Shuttle Radar Topography Mission (SRTM), with a spatial resolution of 1 arcsecond, which corresponds to approximately 30 m at the latitude of the study area. Both the generated interferograms and the resulting mean velocity maps and displacement time series have a spatial resolution of approximately 3 m. For both ascending and descending datasets, a minimum temporal coherence threshold of 0.35 was imposed, and all points with lower coherence values were discarded from the analysis. Further details about the CSK datasets and the SBAS-DInSAR processing chain adopted in this study can be found in [42]. Please note that the referenced documentation is currently available in Italian; an English version will be made available soon.

Each PS location on the Earth's surface is described by WGS84 Latitude, Longitude, and Topography above the ellipsoid. The DInSAR datasets were imported into Geographic Information System (GIS) software, facilitating the organisation and visualisation of data associated with specific positions on the Earth's surface. A significant number of PSs were identified on the Palatino Bridge by analysing the datasets from both orbits (Fig. 8). Additional coherence filters are not applied in this case study. These PSs are distributed homogeneously along the north and south sides of the bridge deck. Negative LOS velocities (red PSs) indicate movement away from the satellite, while positive LOS velocities (blue PSs) indicate movement toward the satellite. Generally, the PSs on the bridge show zero velocity over the observation period (yellow PSs), indicating stability. In this context, velocity is defined as the slope of the best-fitting line through the displacement time series data.

Fig. 8. PSs from the (a-b) ascending and (c-d) descending datasets.

4.3. Results of the analysis

The available InSAR data are employed to analyse the behaviour of the Palatino Bridge and assess the uncertainties associated with its displacements within the proposed theoretical framework. Initially, a regular grid with rectangular cells is used to cluster the PSs. Next, to reduce uncertainties, various approaches are explored in the subsequent section. These include the use of a tailored grid with non-regular cells and the application of an elevation-based filter. Additionally, the impact of the initial normalisation of LOS displacement time histories is discussed. Results are compared in terms of the metrics proposed in Section 3.2.

4.3.1. Regular grid

Initially, a regular grid is used to cluster the PSs covering the Palatino Bridge, as might occur in the context of an automated procedure when prior knowledge of the bridge's features is not available. The grid dimensions are set to 0.0005 degrees in longitude and 0.0001 degrees in latitude, corresponding to rectangles of approximately 40 m in the *E*-direction and 10 m in the N-direction, as shown in Fig. 9. The grid consists of five rectangles covering the north side of the bridge ($n = 1, \ldots, 5$) and five covering the south ($n = 6, \ldots, 10$) one. No filtering is applied to the PSs within these ten areas. The eastern and western ends of the bridge include some PSs from the banks of the Tiber River, while the other areas may contain PSs from both the deck and the piers, as no elevation-based criteria are applied. The number of PSs in each area is displayed in Table 1, ranging from 2 to 62 PSs, together with statistics on PS distributions. The number of PSs from the two orbits is comparable. Specifically, 438 PSs are analysed from the ascending orbit, while 381 PSs are analysed from the descending orbit, for a total of 819 PSs.

The method outlined in Section 2.2, including grid subsampling and linear temporal interpolation, is used to reconstruct the displacements of

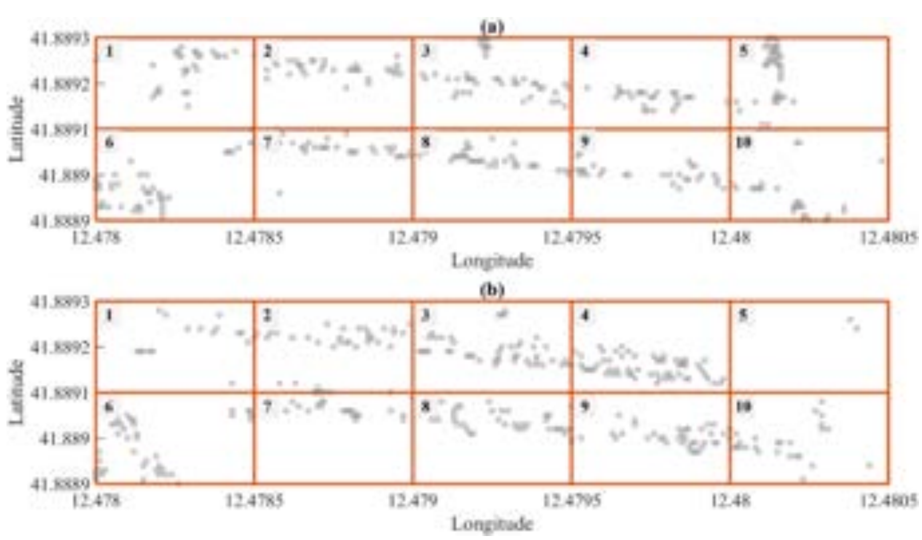

Fig. 9. Clustering of PSs using a regular grid: (a) ascending and (b) descending datasets.

Table 1
PS number across different areas using a regular grid.

Area n	1	2	3	4	5	6	7	8	9	10	Total no.	Mean	S.Dev.
Asc.	36	44	54	33	62	59	42	41	33	34	438	43.8	10.9
Desc.	19	43	53	62	2	51	28	51	44	28	381	38.1	18.4
Overall											819	41.0	15.0

the Bridge in the *E*- and U-directions, with the assumption that displacements in the N-direction are negligible. This assumption is based on the sensor's inability to detect movement along the N-S direction, as discussed earlier in Section 2.1. Furthermore, as detailed in Section 4.1, minimal N-S movement is expected due to the presence of continuous iron beams, which primarily deform in the longitudinal direction—nearly aligned with the E-direction—under the influence of temperature changes. In the remainder of this paper, the term "longitudinal displacements" is used to refer to displacements in the E-direction, as the axis of the bridge is nearly aligned with this direction.

First, the mean displacement time histories are computed for each area and satellite orbit. The mean displacement values from the first two years are subtracted from subsequent observations to enhance result visualisation, ensuring that displacements oscillate around zero. This approach is discussed in further detail in Section 4.3.3. Time histories from both orbits are then interpolated across the entire acquisition timeline to merge datasets obtained at different times. Subsequently, vertical and longitudinal displacements are estimated using eqs. (17) and (19), considering ascending and descending displacements as well as the following coefficients:

- Time invariant coefficients a_E, b_E, a_U, and b_U, computed according to eqs. (5), depending only on the direction cosines characterizing the two acquisition geometries, with values $a_E = 0.946$, $b_E = 1.003$, $a_U = 0.539$, $b_U = -0.631$.
- Time variant coefficients c_1^t and c_2^t, computed according to eqs. (15), depending only on the acquisition times, varying between 0 and 1.

Fig. 10 illustrates the time series of vertical and longitudinal displacements for the ten areas.

The vertical displacements shown in Fig. 10(a) do not exhibit a clear seasonal trend. Most areas display similar behaviour, except for Areas 5, 6, and 10, located at the bridge ends, which show increasing negative displacements over time. This trend is attributed to local subsidence around the abutments, as illustrated in Fig. 8. In a separate study [35], the vertical displacements of the bridge were compared with those of the nearby Roman ruins of the Broken Bridge using InSAR data. The ruins, constructed from marble blocks, move as rigid bodies along with the ground. The comparison revealed a remarkably high consistency between the vertical displacements of the bridge and the ruins, suggesting a shared hydrogeological origin.

Regarding the longitudinal displacements, excluding the end areas (i.e., pairs of Areas 1–6 and 5–10), the north and south sides of the bridge exhibit similar behaviour, with the displacements of paired Areas 2–7, 3–8, and 4–9 being very consistent. Generally, longitudinal displacements are influenced by seasonal trends, particularly temperature fluctuations.

Specifically, the longitudinal displacements of Areas 1, 2, and 7 are in agreement, with maximum displacements occurring in winter and minimum displacements in summer. In contrast, Areas 4, 9, and 10 exhibit displacements with opposite signs. This behaviour can be attributed to the fixed connection between the longitudinal beams of the bridge deck and the masonry pier located on the central piers, corresponding to Areas 3 and 8. As a result, the sections of the bridge on the same side of this fixed connection show concordant displacements. Areas 5, 6, 3, and 8 do not exhibit clear seasonal behaviour. While this

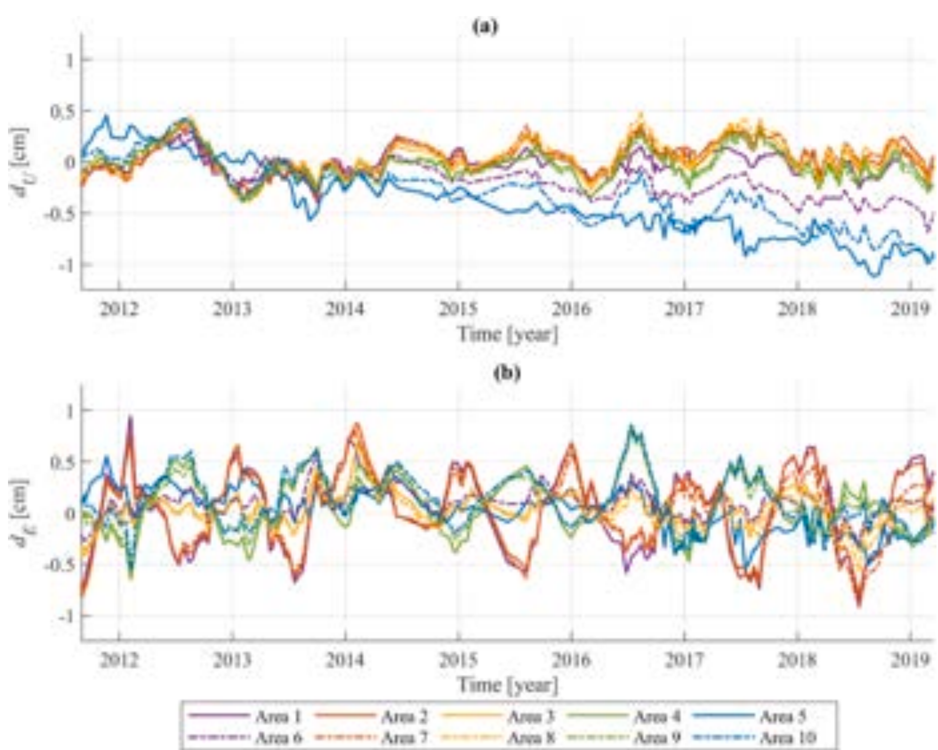

Fig. 10. Reconstructed structural displacements using a regular grid: (a) Vertical and (b) Longitudinal.

lack of seasonal variation is expected for Areas 3 and 8 located in the vicinity of the fixed support, Areas 5 and 6 are expected to display such a trend. Additionally, displacement should increase with distance from the fixed connection, but this pattern is not observed in the data.

The standard deviations associated with the reconstructed structural displacement are shown in Fig. 11. In general, the standard deviations increase over time, indicating that the LOS displacements are progressively diverging. The longitudinal displacements exhibit higher standard deviations than the vertical ones, which is consistent with their larger magnitude. More specifically, the standard deviations of the longitudinal and vertical displacements are determined by the standard deviations of the LOS displacements, the time-invariant coefficients (a_E, b_E, a_U, and b_U), and the time-variant coefficients (c_1^t and c_2^t). While the same LOS displacement standard deviations and time-variant coefficients are applied for both longitudinal and vertical displacement calculations, the time-invariant coefficients a_E and b_E used for longitudinal displacements are larger, in absolute value, than the coefficients a_U and b_U used for vertical displacements. This results in larger standard deviations associated with the longitudinal displacements.

The end areas (i.e., pairs of Areas 1–6 and 5–10) present notably larger standard deviations for both vertical and longitudinal displacements compared to other regions, suggesting the presence of PSs with dissimilar behaviour within these areas. These are the same areas that are showing anomalous longitudinal displacements.

4.3.2. Tailored grid

The combination of anomalous displacement time histories and large standard deviations obtained using a regular grid suggests that an alternative grid configuration should be considered. Given the varying angles between the masonry supports of the bridge (piers and abutments) and the longitudinal axis of the deck, a customised grid is implemented. This approach can only be employed within the context of automated procedures when there exists prior knowledge of the bridge's key features. This grid is designed with areas that cover the north and south sides of the continuous deck between two masonry supports, as illustrated in Fig. 12. Each grid area covers similar sections of the bridge as the previous grid, but with refined dimensions: approximately 30 m in the east-west direction and 10 m in the north-south direction.

The analysis criteria included filtering PSs based not only on their longitude and latitude but also on their altitude, concentrating on those within a narrow strip approximately 5 m wide that corresponds to the bridge deck. The distribution of PSs within these areas is detailed in Table 2, with the number of PSs ranging between 13 and 48. Compared to the previous case using a regular grid, the PSs are more uniformly distributed across the different areas.

The reconstructed structural displacements are displayed in Fig. 13, while the associated standard deviations are presented in Fig. 14. In Fig. 13a, the vertical displacements of Area 6 are consistent with those of the other areas. Although Areas 5 and 10 still exhibit increasing negative displacements over time, the magnitude of these displacements is lower than that shown in Fig. 10a. Regarding the longitudinal displacements, Areas 5 and 6 now display a clear seasonal pattern. Additionally, the displacements increase with distance from the fixed connection: displacements in Areas 1 and 6 are larger than those in Areas 2 and 7, and displacements in Areas 5 and 10 exceed those in Areas 4 and 9. The standard deviations generally decrease across all areas, except for Areas 1 and 6. In Area 1, the standard deviations remain relatively unchanged, whereas in Area 6, they increase significantly. As a result, an in-depth investigation into these areas is required.

Fig. 15 illustrates the time histories of PSs from the ascending orbit belonging to Areas 1 and 6 of the tailored grid. The associated mean displacements are shown in Fig. 16 together with two confidence boundaries: The internal boundary, representing the standard deviation of the sample means ($\pm\sigma_{\mu_{d^t_{LOS,A,n}}}$), and the external one, representing the sample standard deviation ($\pm\sigma_{d^t_{E,n}}$). Visually, two distinct clusters of PSs can be identified in both Areas 1 and 6. The grey clusters exhibit a clear seasonal pattern with velocities close to zero, while the red clusters show a significant negative velocity and negligible seasonal variation.

More in detail, the red cluster in Area 1 comprises four PSs, while the red cluster in Area 6 consists of seven PSs for a total of eleven PSs. The grey clusters can be associated with the west end of the bridge, whereas

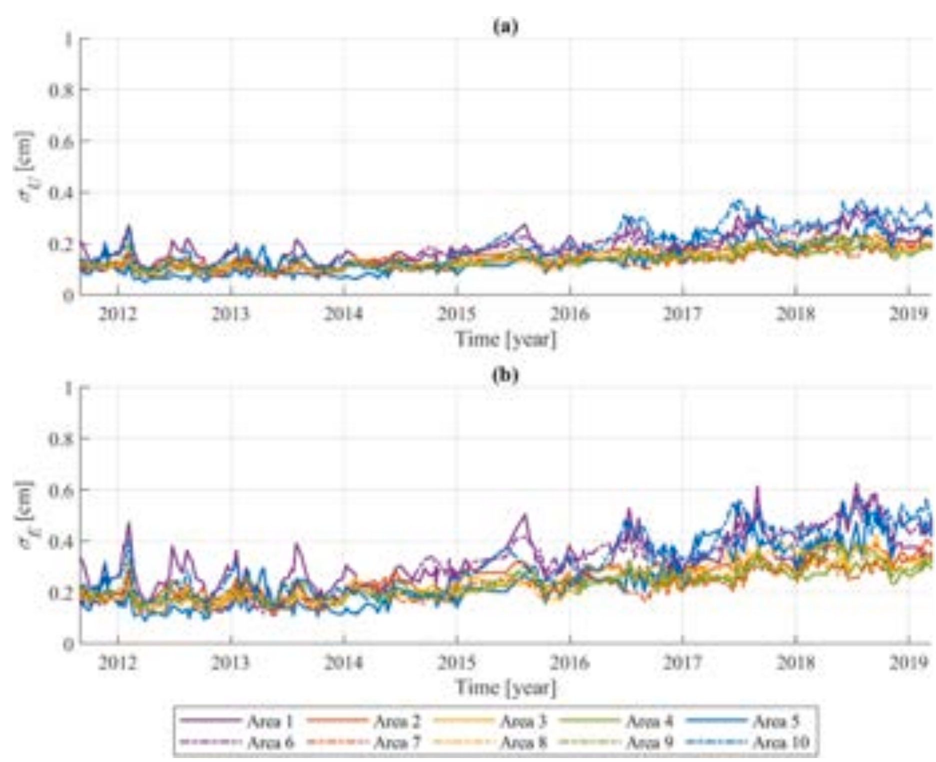

Fig. 11. Error in Reconstructed Structural Displacements: (a) Vertical and (b) Longitudinal.

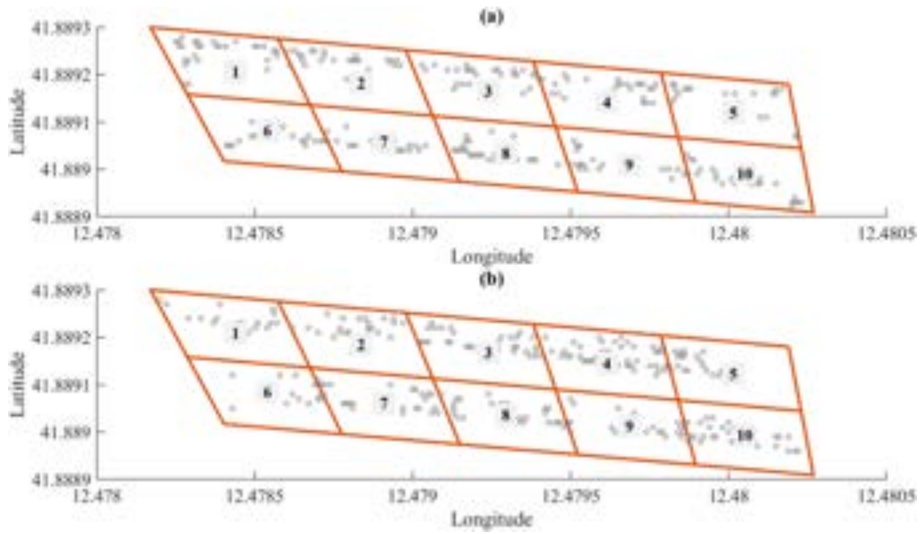

Fig. 12. Clustering of PSs using a tailored grid.

Table 2
PS number across different areas using a tailored grid.

Area n	1	2	3	4	5	6	7	8	9	10	Total no.	Mean	S.Dev.
Asc.	35	30	32	27	28	28	23	34	22	26	285	28.5	4.3
Desc.	19	25	39	48	21	13	29	28	24	31	277	27.7	10.1
Overall											562	28.1	7.5

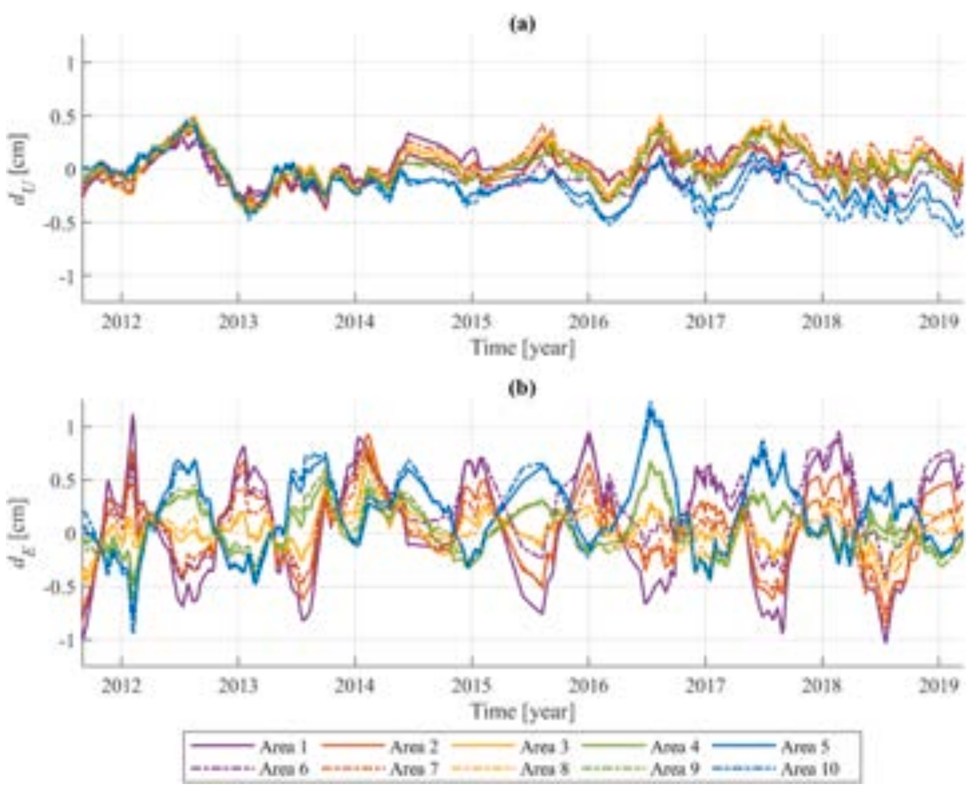

Fig. 13. Reconstructed structural displacements using a tailored grid: (a) Vertical and (b) Longitudinal.

the red cluster corresponds to the adjoining street. As shown in Fig. 15, the PSs with high velocities are located outside the bridge deck, with the joint highlighted in yellow, marking the boundary between the bridge and the road.

As for the sharp increase in standard deviations in Area 6, it can be explained by the fact that, under the regular grid configuration, most of the PSs within this area were not located on the bridge but in the surrounding area, which exhibited relatively homogeneous behaviour that

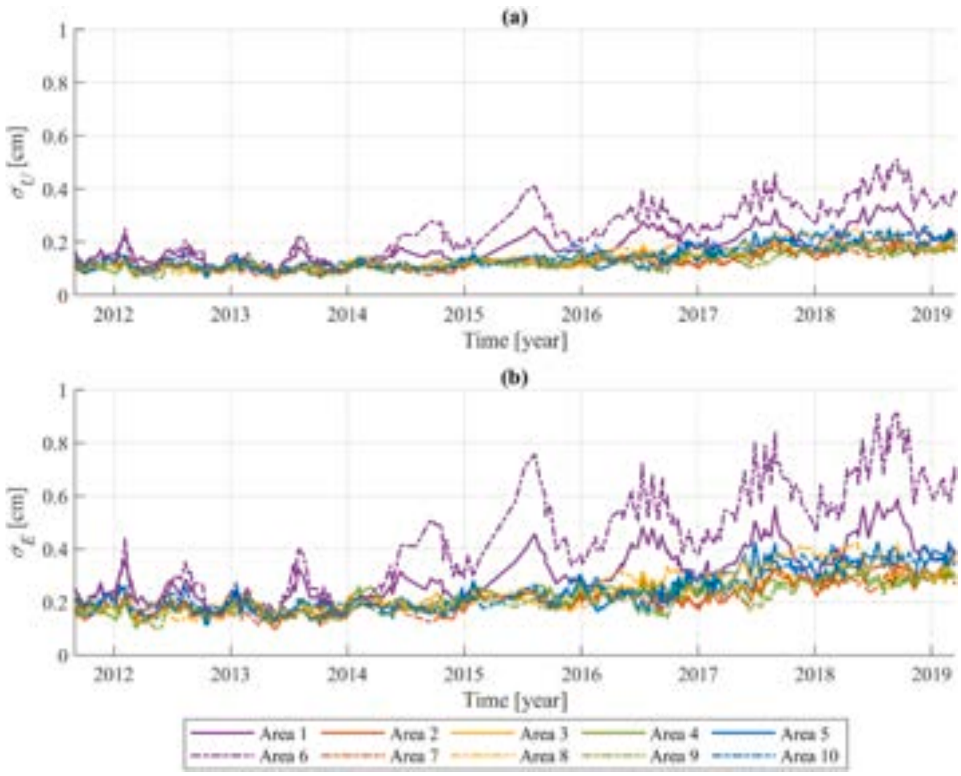

Fig. 14. Reconstructed structural displacements using a tailored grid: (a) Vertical and (b) Longitudinal.

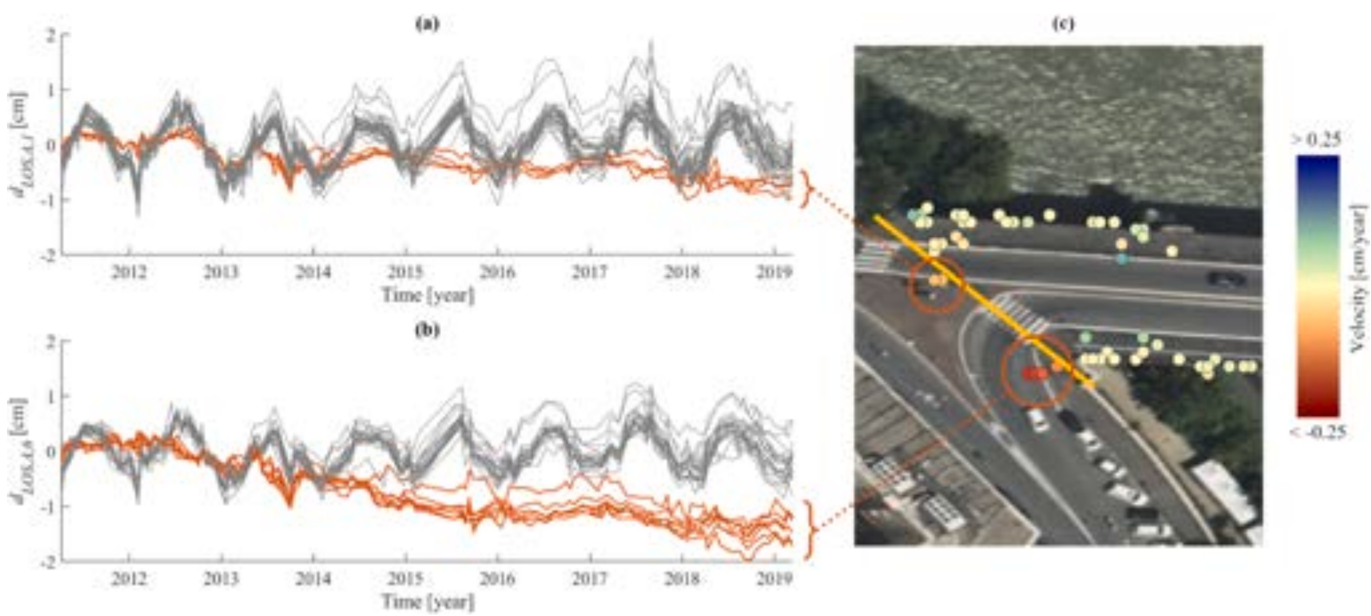

Fig. 15. Identification of two clusters in the time histories of PSs from the ascending orbit belonging to (a) Area 1 and (b) Area 6 of the tailored grid; (c) zoom on the two areas showing PS velocities. The joint between the road and the bridge is highlighted in yellow. (For interpretation of the references to colour in this figure legend, the reader is referred to the web version of this article.)

did not represent the bridge's displacements. In contrast, the new Area 6 contains both PSs from the bridge and those from the surrounding area, resulting in two distinct clusters of PSs. Consequently, the standard deviations increase because the PSs in this area cannot be attributed to the same quantity.

Fig. 17 further examines this aspect by displaying the correlation matrices, which show the Pearson Correlation Coefficients (PCC) between the displacement time histories of the PSs from the ascending orbit in Areas 1 and 6. The PCC measures the linear correlation between two variables, ranging from -1 to $+1$, where $+1$ indicates a perfect positive linear correlation, -1 signifies a perfect negative linear correlation, and 0 denotes no linear correlation. Initially, the PSs are ordered by their ID (matrices on the left), making it challenging to distinguish clusters. However, when the PSs are sorted by their velocity in ascending order (matrices on the right), two distinct clusters become evident based on the correlation values.

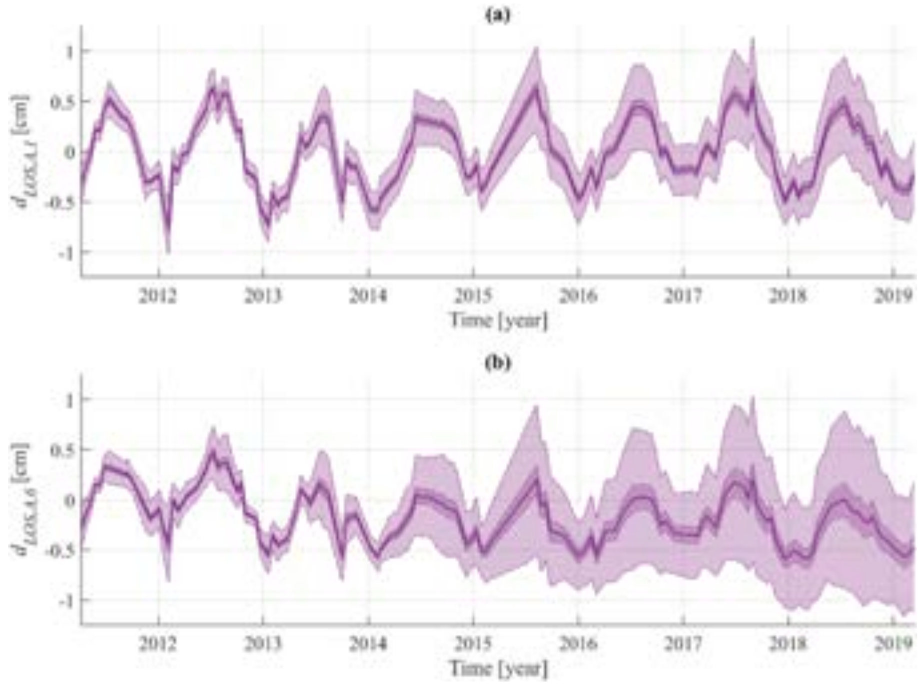

Fig. 16. Time histories of PSs from the Ascending orbit belonging to (a) Area 1 and (b) Area 6 with associated confidence boundary ($\pm\sigma_{d^t_{E,n}}$) obtained using a tailored grid. The internal boundary represents the standard deviation of the sample means ($\pm\sigma_{\mu_{d^t_{LOS,A,n}}}$).

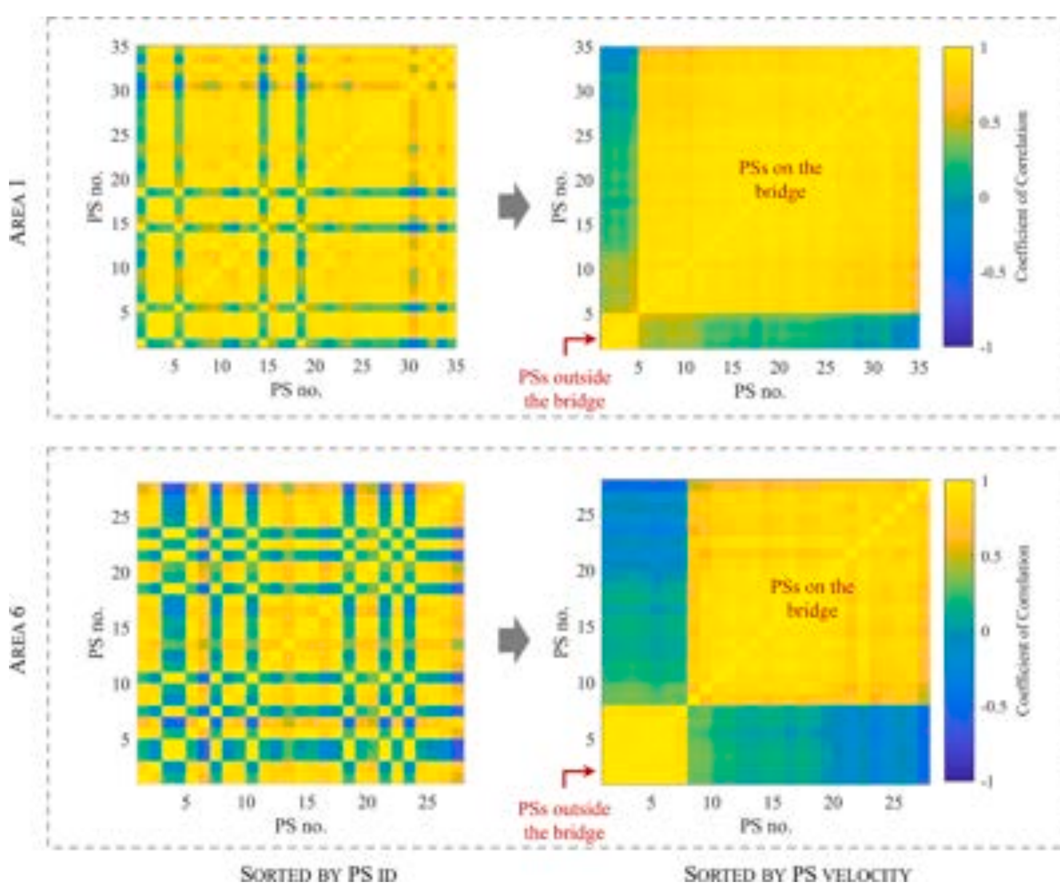

Fig. 17. Correlation matrices between displacement time histories.

Table 3
PS number across different areas using a tailored grid (after PS selection).

Area n	1	2	3	4	5	6	7	8	9	10	Total	Mean	S.Dev.
Asc.	31	30	32	27	28	21	23	34	22	26	274	27.4	4.3
Desc.	19	25	39	48	21	13	29	28	24	31	277	27.7	10.1
Overall											551	27.6	7.6

Based on these considerations, the eleven PSs from the ascending orbit that are not located on the bridge are excluded from the analysis, and the remaining PSs, detailed in Table 3, are used to repeat the analysis.

The reconstructed structural displacements are shown in Fig. 18, with the corresponding standard deviations in Fig. 19. Areas 1 and 6 exhibit similar displacement time histories. The displacements in Area 6 are slightly smaller than in Area 1, reflecting the difference in the length of the longitudinal beams on the north (longer beams) and south (shorter beams) sides of the bridge. The standard deviations of both vertical (Fig. 19a) and longitudinal (Fig. 19b) displacements are now consistent across different areas. Fig. 20 presents the same results as Fig. 16, with the PSs outside the bridge being removed. The reduction in both the sample standard deviation and the standard deviation of the sample means of Areas 1 and 6 is significant and evident. Fig. 21 displays the mean standard deviation associated with the three grid configurations considered computed according to eqs. (25) and (26), which provides a global representation of the uncertainty affecting the structural displacements in the three cases considered.

4.3.3. Impact of LOS displacement normalisation

The displacement time series are expressed as differential values, with all measurements referenced to the first acquisition, which is commonly set to zero. However, typically, SAR image acquisitions for ascending and descending geometries are temporally offset. To deal with this issue, the standard approach, as discussed by Talledo et al. [27], involves trimming the time series of the earlier acquisition to ensure both datasets share a common starting point. Following this, the displacement time series should be adjusted by accounting for the cumulative displacement recorded at the trimming point.

In this study, a non-conventional displacement normalisation approach is adopted, where the LOS time series are adjusted by subtracting the mean displacement observed during the first two years, ensuring that displacements oscillate around zero. This two-year reference period is chosen as a compromise between two key objectives: first, to account for cyclic displacements driven by seasonal temperature variations; and second, to detect and highlight anomalous trends, such as increasing displacement velocities over time, as observed in the vertical displacements of Areas 5 and 10. The two-year period is particularly effective in balancing intra-year variations, which reflect seasonal expansion and contraction, and inter-year variations, which account for fluctuations in annual temperature cycles.

For this case study, the chosen normalisation method improves the visualisation of displacement trends, facilitating the distinction between periodic seasonal effects and potential long-term structural changes. However, this approach may not be suitable for all scenarios. If a structure experiences high displacement velocities during the initial reference period, subtracting the mean displacement over this timeframe could lead to misinterpretations, as the assumption of oscillation around zero would no longer be valid.

Fig. 22 illustrates how the outcomes presented in Fig. 18 (which includes vertical and longitudinal structural displacements obtained considering a tailored grid, elevation-based filtering, and eliminating PSs not associated with the bridge) would appear if initial displacements were set to zero at the trimming point. It is noteworthy that, in this case, the time history for the ascending data begins before that of the

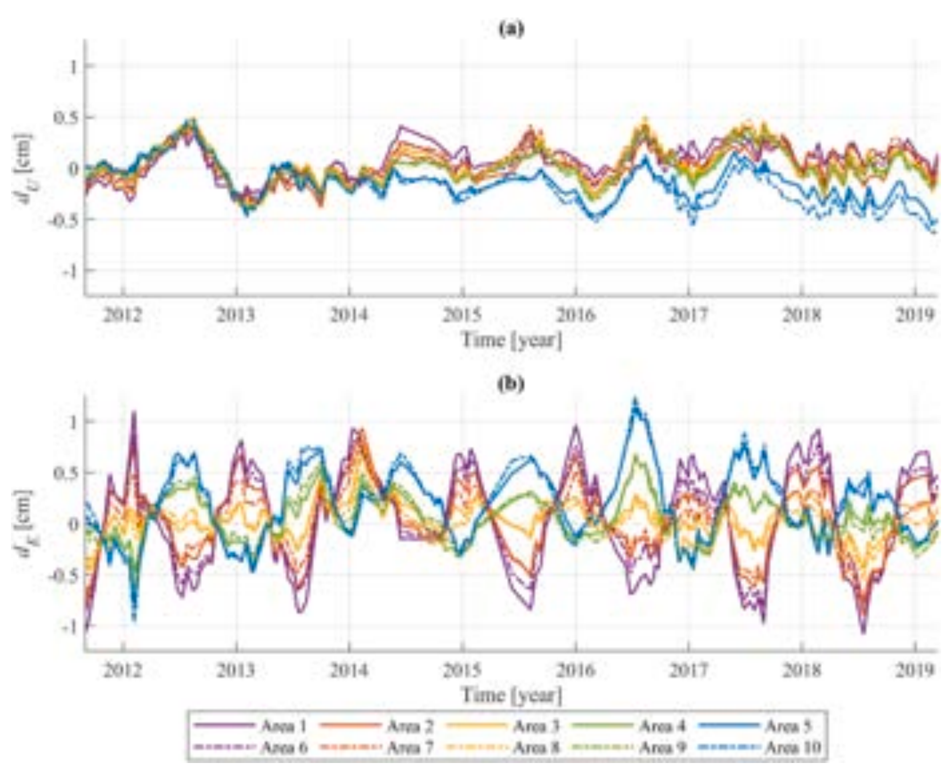

Fig. 18. Reconstructed structural displacements using a tailored grid, removing PSs outside the bridge: (a) Vertical and (b) Longitudinal.

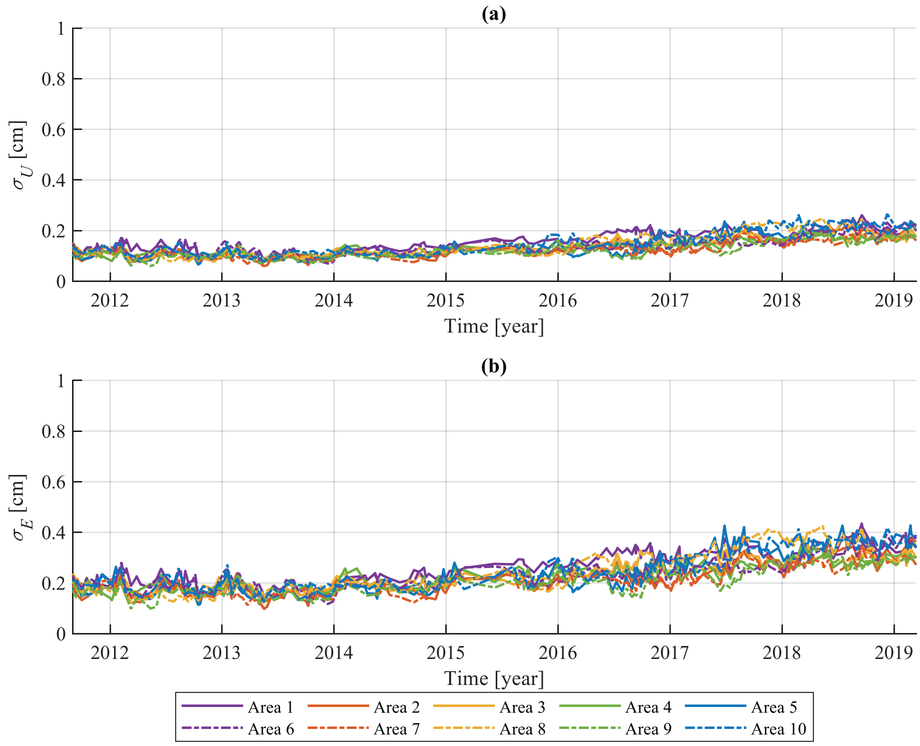

Fig. 19. Error of the reconstructed structural displacements using a tailored grid, removing PSs outside the bridge: (a) Vertical and (b) Longitudinal.

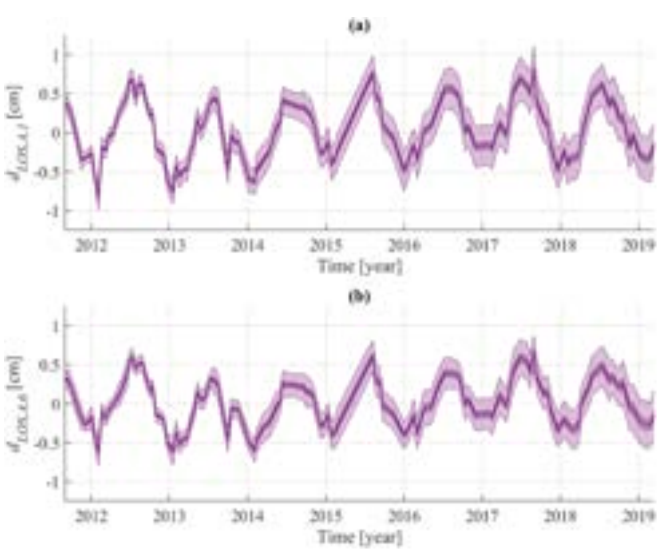

Fig. 20. Time histories of PSs from the Ascending orbit belonging to (a) Area 1 and (b) Area 6 with associated confidence boundary ($\pm\sigma_{d^{r}_{E,n}}$) obtained using a tailored grid and removing PSs outside the bridge. The internal boundary represents the standard deviation of the sample means ($\pm\sigma_{\mu_{d^{r}_{LOS,A,n}}}$).

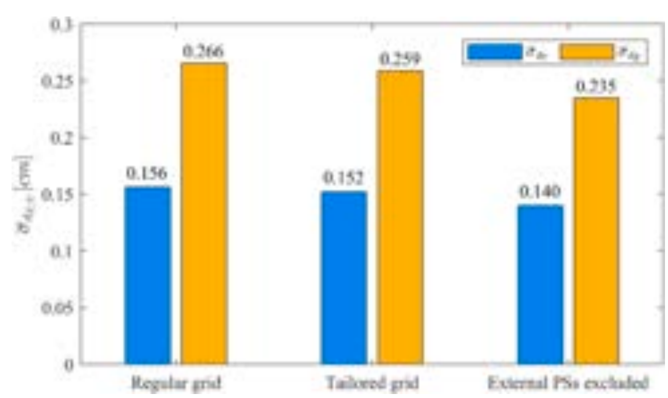

Fig. 21. Mean standard deviations associated with different grid configurations.

descending data. Consequently, the ascending data were trimmed to align with the starting point of the descending data, ensuring that the initial displacement for each PS is zero at that moment.

Following this common approach, particularly for longitudinal displacements, the interpretation of the bridge's behaviour would become significantly more complex. Specifically: 1) Displacements oscillate around an offset that lacks physical significance and merely reflects the chosen starting point of the observation; 2) The increase in displacement with distance from the fixed point of the deck is not easily discernible; 3) Negative and positive variations due to thermal fluctuations are obscured, as displacements predominantly appear positive due to the initial offset.

Importantly, the choice of initial normalisation affects the standard deviations of the reconstructed displacements. Fig. 23 displays the standard deviations associated with the displacements depicted in Fig. 22, revealing that they are generally higher than those shown in Fig. 19.

Fig. 24 presents the time history of longitudinal displacements in Area 1 under two different normalisation scenarios: the mean displacement over the first two years set to zero (Fig. 24(a)) and the initial displacement set to zero (Fig. 24(b)). The latter approach results in greater uncertainty; while initial displacements are uniformly set to zero, their differences tend to increase over time.

To provide a quantitative representation of the uncertainty affecting the displacements of Area 1 for the two cases considered, Fig. 25 shows the mean standard deviations over the observation period, which is maximum for case 2.

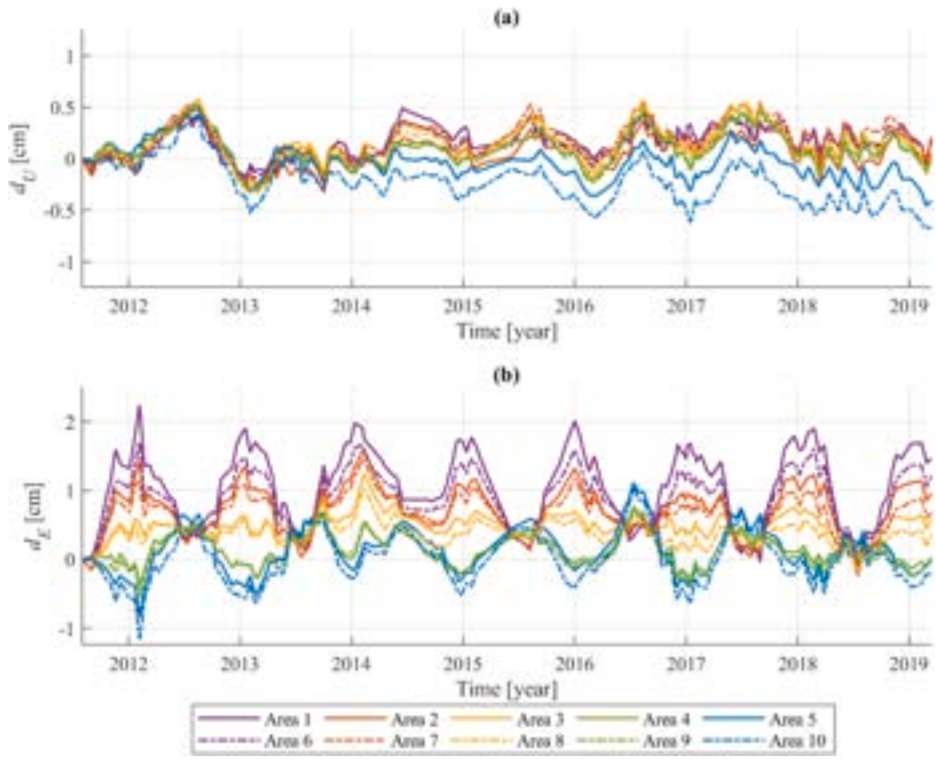

Fig. 22. Reconstructed structural displacements considering null initial LOS displacements: (a) Vertical and (b) Longitudinal.

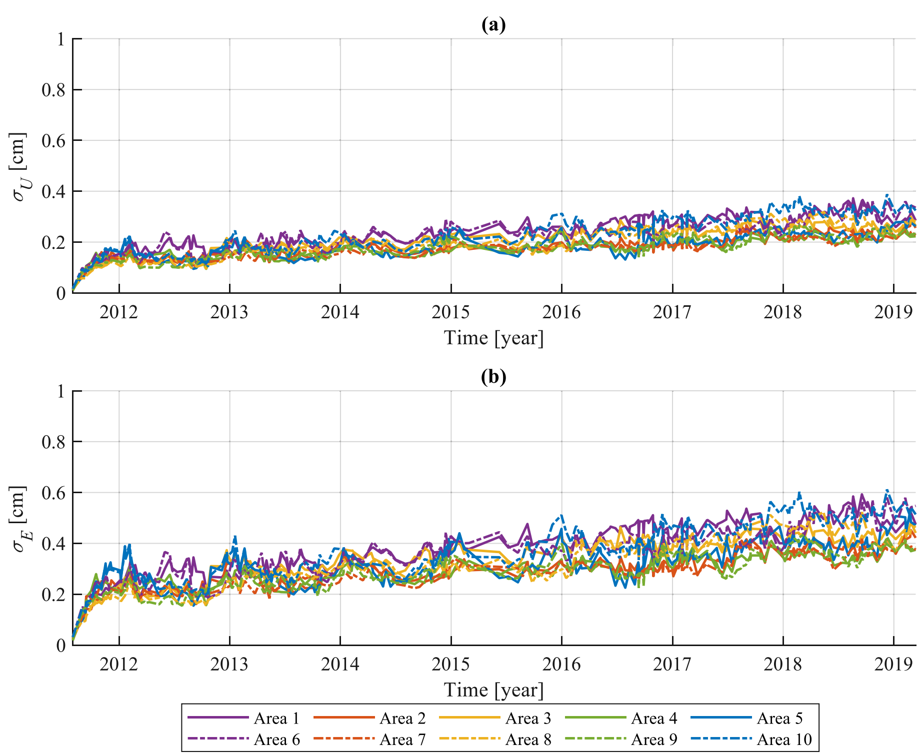

Fig. 23. Error of the reconstructed structural displacements considering null initial LOS displacements: (a) Vertical and (b) Longitudinal.

5. Discussion

This section discusses the performance of the proposed framework, compares it with existing InSAR-based monitoring methods, addresses its limitations, and outlines potential future enhancements to improve scalability and practical efficacy.

This study investigated the influence of spatial and temporal resampling on the uncertainty of InSAR-derived structural displacements and proposed a framework to quantify and reduce this variability. The results of the case study demonstrate that processing decisions, such as grid layout, affect the precision of displacement estimates and should not be made arbitrarily. The case study demonstrated that adapting the

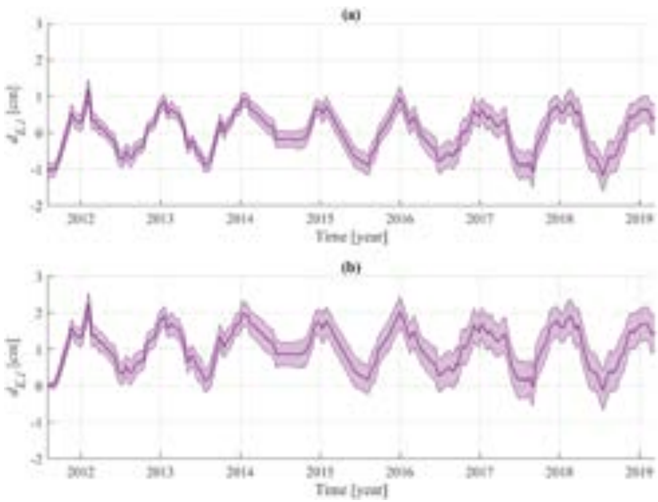

Fig. 24. Effect of initial standardisation of PS displacement time series: (a) tailored normalisation (mean displacement in the first two years equal to zero); (b) Typical normalisation (initial displacement equal to zero).

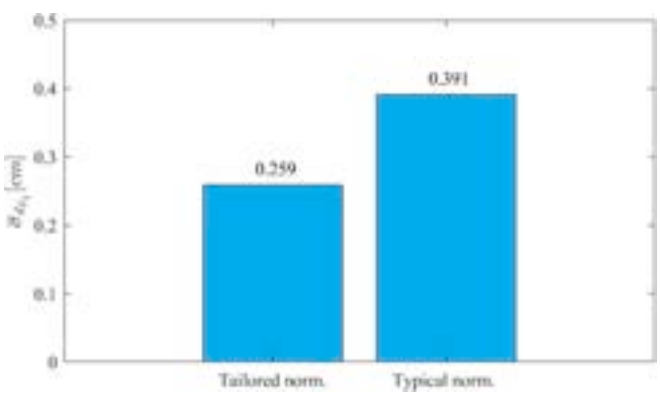

Fig. 25. Mean standard deviations over the observation period for Area 1.

grid layout to the geometry of the structure and the spatial distribution of PSs enhances the consistency of displacement measurements. Across the entire bridge, replacing a fixed regular grid with a tailored configuration led to a reduction of approximately 12 % in the mean standard deviation of displacements, as shown in Fig. 21. On a more local scale, a comparison between Fig. 14 and Fig. 19 shows that, for Zone 6, filtering out PSs not physically located on the structure reduced the mean standard deviation over time by up to 45 % for longitudinal displacements and 42 % for vertical displacements. Similar improvements were observed in Zone 1, where the reductions were 13 % and 11 % for the longitudinal and vertical components, respectively. These results underscore the practical utility of the proposed framework in supporting informed decisions on grid design and PS selection, ultimately improving the reliability of InSAR-derived structural displacement estimates.

In comparison to the state-of-the-art, the main distinctions and contributions of this work can be summarised as follows: 1) Most InSAR studies rely on fixed or arbitrarily defined spatial grids, without assessing how the choice of grid geometry affects displacement variability. In contrast, our framework explicitly quantifies the impact of grid layout and proposes metrics for optimisation. 2) While conventional MT-InSAR techniques (e.g., PSI, SBAS) provide pixel-level coherence or error estimates, they rarely assess the uncertainty introduced by temporal interpolation and spatial aggregation. Our method directly targets this gap by analysing how these processing steps propagate uncertainty. 3) Existing studies often focus on maximising the number of PSs for spatial coverage. Our approach emphasises the statistical consistency of grouped PSs, demonstrating that tailored PS clustering can reduce variability even at the cost of fewer points. 4) While previous studies [9] have focused on the uncertainty introduced by assuming one displacement component to be zero when combining ascending and descending datasets, our work addresses a complementary issue: the uncertainty arising from spatial and temporal resampling of the data.

Nonetheless, the framework has several limitations. The variability of individual displacement observations is influenced by several factors inherent to InSAR data, including measurement noise, residual atmospheric effects, temporal and spatial decorrelation, and phase unwrapping errors. While measurement noise and atmospheric conditions contribute to random variability, unwrapping errors and orbital inaccuracies can introduce systematic biases that distort displacement estimates. These biases affect the mean values and cannot be mitigated through averaging. Although the preprocessing workflow can exclude datasets with obvious unwrapping issues, a full quantification of bias would require external reference data, such as GNSS measurements, which is beyond the scope of this work. Furthermore, the current implementation evaluates only a discrete set of grid configurations and does not yet include automated or adaptive optimisation, which may limit its flexibility in complex monitoring scenarios. From a practical standpoint, the application of this framework is subject to the physical constraints of InSAR monitoring. It requires structures that are large enough to contain a sufficient number of PSs, which may not be feasible for small or vegetation-covered assets. Metal and concrete surfaces provide better radar returns, making the method more effective for infrastructure such as bridges, towers, and high-rise buildings. However, in dense urban settings, PSs are often located on rooftops rather than on structural elements, which can limit interpretability. Additionally, because InSAR is most sensitive to gradual, continuous displacements, it may not be suitable for detecting abrupt or brittle failure mechanisms.

Despite these limitations, the framework provides a practical and transferable method for evaluating uncertainty propagation due to spatial and temporal resampling, an aspect that is often overlooked in existing studies. By offering insight into how processing choices affect displacement reliability, it supports more informed decision-making in large-scale, automated structural monitoring applications.

Finally, we present considerations for automating grid optimisation and PS selection. As grid cell dimensions increase, a larger number of PSs is typically included, which may result in greater variability among individual displacement measurements. Conversely, when a cell contains only a small number of PSs, the standard deviation of the mean displacement increases, reducing the reliability of the estimate. Balancing these competing effects requires the formulation of an objective function that maximises the number of PSs within each cell while minimising the uncertainty associated with the estimated displacement. In addition, cell dimensions must respect the spatial resolution of the satellite; cells smaller than this limit cannot ensure meaningful averaging of displacement time series. The choice of optimisation strategy also depends on the type of grid and the specific goals of the analysis. Regular grids are designed to ensure uniform spatial coverage and typically involve optimising the number of cells along latitude and longitude. In contrast, structure-aligned grids—such as those following the axis of linear infrastructures like roads or railways—must accommodate application-specific design criteria. For instance, to capture asymmetric structural behaviour, it is necessary to include at least one cell on each side of the structure. In such cases, while the cell width may be constrained by the geometry of the monitored structure, the cell length along the longitudinal axis should be optimised according to the same PS- and uncertainty-aware principles.

6. Conclusion

As the demand for efficient, automated and reliable infrastructure monitoring grows, recent advancements in satellite-based InSAR monitoring have paved the way for automated inspection applications, particularly in network-scale analyses. This study presented a framework for quantifying uncertainty in InSAR-derived deformation measurements, addressing the challenges of integrating data from different satellite orbits and applying automated resampling techniques to obtain consistent data in space and time. Specifically, by utilising classical error propagation theory, we evaluated how spatial and temporal resampling, specifically through grid subsampling and linear temporal interpolation, affect the precision of reconstructed structural displacements.

In addition to addressing spatial and temporal resampling challenges, the study emphasises the importance of optimising grid configurations and PS selection to obtain meaningful structural displacements and minimise overall uncertainty in displacement measurements. The proposed metrics for assessing uncertainty across various grid configurations, from automatically determined grids to tailored ones, help identify optimal parameters for InSAR data processing, such as grid size and dimensions. Generally, grid configurations with lower uncertainty suggest that the PSs within each area exhibit similar behaviour, supporting the assumption that they represent the same random quantity and can be averaged. Conversely, areas with higher standard deviations compared to neighbouring regions should be carefully examined, as elevated uncertainty may indicate either anomalous displacement in part of the structure or improper clustering of PSs, where the scatterers belong to different objects on the Earth's surface.

The formulated theoretical framework was applied to the case study of the Palatino Bridge in Rome, Italy, a continuous metal truss deck supported by masonry piers. The bridge exhibits noticeable displacements primarily driven by temperature variations. These displacements were calculated using COSMO-SkyMed data, acquired over an extended period from July 2011 to March 2019.

This analysis demonstrated that grid configuration is a critical factor influencing the precision of displacement estimates. The shift from a regular grid to a tailored grid, designed to align with the spatial distribution of PSs, significantly improved the consistency and precision of the displacement data. The tailored grid approach, by better accommodating the physical characteristics of the bridge and the distribution of PSs, reduced the standard deviation of the reconstructed displacements and provided a better representation of structural movements. In some areas of the bridge, elevated standard deviations were observed. Upon closer examination, these areas were found to contain PSs with anomalous behaviour, which were subsequently excluded from the analysis as they were located outside the bridge.

Overall, this work underscores the necessity of rigorous uncertainty assessment to ensure meaningful deformation measurements, which are critical for informed decision-making in infrastructure monitoring and maintenance. This is especially important for automated monitoring procedures, where the characteristics of the grid are fixed in advance.

This study lays the foundation for reliability-based analyses of civil structures and infrastructures using InSAR data, representing a promising yet underexplored area. By improving uncertainty characterisation and refining processing techniques, future advancements in this field could significantly enhance the robustness of InSAR-based structural health monitoring, facilitating automated and scalable solutions for infrastructure assessment and early warning applications.

Future studies should focus on extending this framework to incorporate alternative spatial and temporal resampling methods, further enhancing its adaptability to various monitoring scenarios. Additionally, the development of automatic optimisation procedures for grid selection and resampling strategies could further improve the efficiency and reliability of uncertainty quantification. Integrating multi-sensor data fusion approaches, such as GNSS or other remote sensing techniques, could also provide a more comprehensive assessment of both uncertainty and bias.

CRediT authorship contribution statement

Pier Francesco Giordano: Writing – original draft, Visualization, Software, Methodology, Conceptualization. **Antonios Kamariotis:** Writing – review & editing, Methodology, Conceptualization. **Giorgia Giardina:** Writing – review & editing, Methodology, Conceptualization. **Eleni Chatzi:** Writing – review & editing, Methodology, Conceptualization. **Maria Pina Limongelli:** Writing – review & editing, Methodology, Conceptualization.

Declaration of competing interest

The authors declare that they have no known competing financial interests or personal relationships that could have appeared to influence the work reported in this paper.

Acknowledgements

Dr. Giordano and Prof. Limongelli carried out this study within the RETURN Extended Partnership and received funding from the European Union Next-GenerationEU (National Recovery and Resilience Plan – NRRP, Mission 4, Component 2, Investment 1.3 – D.D. 1243 2/8/2022, PE0000005). Dr. Giordano would like to thank the IDEA League for funding to enable this collaboration. Prof. Giardina was supported by the Dutch Research Council (NWO), InStruct Vidi project 18912. Prof. Chatzi gratefully acknowledges the funding from the Swiss National Science Foundation (SNSF) under the Horizon Europe funding guarantee, for the project 'ReCharged - Climate-aware Resilience for Sustainable Critical and interdependent Infrastructure Systems enhanced by emerging Digital Technologies' (grant agreement No: 101086413). CNR-IREA is gratefully acknowledged for processing and providing InSAR-derived data.

Appendix A. Error propagation

Let $y = f(x_1, \ldots, x_k)$ be a differentiable function of k measured random variables, each with means $\mu_{x_1}, \ldots, \mu_{x_k}$ and standard deviations $\sigma_{x_1}, \ldots, \sigma_{x_k}$. By conducting p direct measurements for each variable, a distribution of y values is generated from the different realizations of these random variables. To compute the expected value μ_y and the standard deviation σ_y of y, we use the Taylor expansion to approximate the function $f(x_1, \ldots, x_k)$ in the neighbourhood of the mean values $\mu_{x_1}, \ldots, \mu_{x_k}$. This neighbourhood represents a region where the function behaves sufficiently smoothly so that the linear approximation holds, making the expansion valid. By retaining only the linear terms in this region, the approximation simplifies the computation, yielding:

$$y_i = f(x_{1i}, \ldots, x_{ki}) \approx f\left(\mu_{x_1}, \ldots, \mu_{x_k}\right) + \sum_{j=1}^{k} \left(\frac{\partial f}{\partial x_j}\right)_{x_j=\mu_{x_j}} \left(x_{ji} - \mu_{x_j}\right) \tag{27}$$

where x_{ji} is the i-th measurement of the j-th variable.

This approximation is valid as long as the variables $x_1, \ldots, x_k$ remain close to their mean values, ensuring that higher-order terms are negligible. By applying the definition of mean value of y, we obtain the following expression:

$$\mu_y = \frac{\sum_{i=1}^{n} f(x_{1i}, \ldots, x_{ki})}{p} = \frac{pf\left(\mu_{x_1}, \ldots, \mu_{x_k}\right) + \sum_{i=1}^{p}\sum_{j=1}^{k}\left(\frac{\partial f}{\partial x_j}\right)_{x_j=\mu_{x_j}}\left(x_{ji} - \mu_{x_j}\right)}{p} \tag{28}$$

Since $\sum_{i=1}^{p}\left(x_{ji} - \mu_{x_j}\right) = 0$ for all $j = 1, \ldots, k$, the mean value simplifies to:

$$\mu_y = f\left(\mu_{x_1}, \ldots, \mu_{x_k}\right) \tag{29}$$

Similarly, the standard deviation is obtained as:

$$\sigma_y^2 = \frac{\sum_{i=1}^{p}\left(y_i - \mu_y\right)^2}{p-1} = \frac{\sum_{i=1}^{p}\left[\sum_{j=1}^{k}\left(\frac{\partial f}{\partial x_j}\right)\left(x_{ji} - \mu_{x_j}\right)\right]^2}{p-1} = \frac{\sum_{i=1}^{p}\left[\sum_{j=1}^{k}\left(\frac{\partial f}{\partial x_j}\right)^2\left(x_{ji} - \mu_{x_j}\right)^2 + 2\sum_{l=1}^{k-1}\sum_{m=l+1}^{k}\left(\frac{\partial f}{\partial x_l}\right)\left(\frac{\partial f}{\partial x_m}\right)\left(x_{li} - \mu_{x_l}\right)\left(x_{mi} - \mu_{x_m}\right)\right]}{p-1} \tag{30}$$

In the case of independent variables, the second part of the last expression containing the covariance terms is equal to zero. The standard deviation becomes:

$$\sigma_y^2 = \sum_{j=1}^{k}\left(\frac{\partial f}{\partial x_j}\right)^2\sigma_{x_j}^2 \tag{31}$$

Data availability

The authors do not have permission to share data.

References

[1] Y. An, E. Chatzi, S.H. Sim, S. Laflamme, B. Blachowski, J. Ou, Recent progress and future trends on damage identification methods for bridge structures, Struct. Control. Health Monit. (2019), https://doi.org/10.1002/stc.2416.

[2] C.R. Farrar, K. Worden, An introduction to structural health monitoring, Philos. Trans. R. Soc. A Math. Phys. Eng. Sci. (2007), https://doi.org/10.1098/rsta.2006.1928.

[3] Á. Cunha, E. Caetano, F. Magalhães, C. Moutinho, Dynamic identification and continuous dynamic monitoring of bridges: different applications along bridges life cycle, Struct. Infrastruct. Eng. 14 (2018) 445–467, https://doi.org/10.1080/15732479.2017.1406959.

[4] A. Ferretti, C. Prati, F. Rocca, Nonlinear subsidence rate estimation using permanent scatterers in differential SAR interferometry, IEEE Trans. Geosci. Remote Sens. 38 (2000) 2202–2212, https://doi.org/10.1109/36.868878.

[5] P. Berardino, G. Fornaro, R. Lanari, E. Sansosti, A new algorithm for surface deformation monitoring based on small baseline differential SAR interferograms, IEEE Trans. Geosci. Remote Sens. 40 (2002) 2375–2383, https://doi.org/10.1109/TGRS.2002.803792.

[6] S. Laflamme, F. Ubertini, A. Di Matteo, A. Pirrotta, M. Perry, Y. Fu, J. Li, H. Wang, T. Hoang, B. Glisic, L.J. Bond, M. Pereira, Y. Shu, K.J. Loh, Y. Wang, S. Ding, X. Wang, X. Yu, B. Han, Y. Goldfeld, D. Ryu, R. Napolitano, F. Moreu, G. Giardina, P. Milillo, Roadmap on measurement technologies for next generation structural health monitoring systems, Meas. Sci. Technol. 34 (2023) 093001, https://doi.org/10.1088/1361-6501/acd135.

[7] V. Macchiarulo, P. Milillo, C. Blenkinsopp, C. Reale, G. Giardina, Multi-temporal InSAR for transport infrastructure monitoring: recent trends and challenges, Proc. Inst. Civ. Eng. - Bridg. Eng. 176 (2023) 92–117, https://doi.org/10.1680/jbren.21.00039.

[8] Q. Huang, O. Monserrat, M. Crosetto, B. Crippa, Y. Wang, J. Jiang, Y. Ding, Displacement monitoring and health evaluation of two bridges using Sentinel-1 SAR images, Remote Sens. 10 (2018) 1714, https://doi.org/10.3390/rs10111714.

[9] E. Farneti, N. Cavalagli, M. Costantini, F. Trillo, F. Minati, I. Venanzi, F. Ubertini, A method for structural monitoring of multispan bridges using satellite InSAR data with uncertainty quantification and its pre-collapse application to the Albiano-Magra bridge in Italy, Struct. Health Monit. (2022) 147592172210836, https://doi.org/10.1177/14759217221083609.

[10] F. Di Carlo, A. Miano, I. Giannetti, A. Mele, M. Bonano, R. Lanari, A. Meda, A. Prota, On the integration of multi-temporal synthetic aperture radar interferometry products and historical surveys data for buildings structural monitoring, J. Civ. Struct. Heal. Monit. 11 (2021) 1429–1447, https://doi.org/10.1007/s13349-021-00518-4.

[11] N. Cavalagli, A. Kita, S. Falco, F. Trillo, M. Costantini, F. Ubertini, Satellite radar interferometry and in-situ measurements for static monitoring of historical monuments: the case of Gubbio, Italy, Remote Sens. Environ. 235 (2019) 111453, https://doi.org/10.1016/j.rse.2019.111453.

[12] N.M. Rana, K.B. Delaney, S.G. Evans, E. Deane, A. Small, D.A.M. Adria, S. McDougall, N. Ghahramani, W.A. Take, Application of Sentinel-1 InSAR to monitor tailings dams and predict geotechnical instability: practical considerations based on case study insights, Bull. Eng. Geol. Environ. 83 (2024) 204, https://doi.org/10.1007/s10064-024-03680-3.

[13] P. Milillo, D. Perissin, J.T. Salzer, P. Lundgren, G. Lacava, G. Milillo, C. Serio, Monitoring dam structural health from space: insights from novel InSAR techniques and multi-parametric modeling applied to the Pertusillo dam Basilicata, Italy, Int. J. Appl. Earth Obs. Geoinf. 52 (2016) 221–229, https://doi.org/10.1016/j.jag.2016.06.013.

[14] G. Giardina, P. Milillo, M.J. DeJong, D. Perissin, G. Milillo, Evaluation of InSAR monitoring data for post-tunnelling settlement damage assessment, Struct. Control. Health Monit. 26 (2019), https://doi.org/10.1002/stc.2285.

[15] B. Bayer, A. Simoni, D. Schmidt, L. Bertello, Using advanced InSAR techniques to monitor landslide deformations induced by tunneling in the northern Apennines, Italy, Eng. Geol. 226 (2017) 20–32, https://doi.org/10.1016/j.enggeo.2017.03.026.

[16] M. Koohmishi, S. Kaewunruen, L. Chang, Y. Guo, Advancing railway track health monitoring: integrating GPR, InSAR and machine learning for enhanced asset management, Autom. Constr. 162 (2024) 105378, https://doi.org/10.1016/j.autcon.2024.105378.

[17] L. Chang, R.P.B.J. Dollevoet, R.F. Hanssen, Nationwide railway monitoring using satellite SAR interferometry, IEEE J. Sel. Top. Appl. Earth Obs. Remote Sens. 10 (2017) 596–604, https://doi.org/10.1109/JSTARS.2016.2584783.

[18] P. Milillo, G. Giardina, D. Perissin, G. Milillo, A. Coletta, C. Terranova, Pre-collapse space geodetic observations of critical infrastructure: the Morandi bridge, Genoa, Italy, Remote Sens. 11 (2019) 1403, https://doi.org/10.3390/rs11121403.

[19] S. Selvakumaran, S. Plank, C. Geiß, C. Rossi, C. Middleton, Remote monitoring to predict bridge scour failure using interferometric synthetic aperture radar (InSAR) stacking techniques, Int. J. Appl. Earth Obs. Geoinf. 73 (2018) 463–470, https://doi.org/10.1016/j.jag.2018.07.004.

[20] J.J. Sousa, L. Bastos, Multi-temporal SAR interferometry reveals acceleration of bridge sinking before collapse, Nat. Hazards Earth Syst. Sci. 13 (2013) 659–667, https://doi.org/10.5194/nhess-13-659-2013.

[21] V. Macchiarulo, P. Milillo, C. Blenkinsopp, G. Giardina, Monitoring deformations of infrastructure networks: a fully automated GIS integration and analysis of InSAR time-series, Struct. Health Monit. 21 (2022) 1849–1878, https://doi.org/10.1177/14759217211045912.

[22] A. Nettis, V. Massimi, R. Nutricato, D.O. Nitti, S. Samarelli, G. Uva, Satellite-based interferometry for monitoring structural deformations of bridge portfolios, Autom. Constr. 147 (2023) 104707, https://doi.org/10.1016/j.autcon.2022.104707.

[23] A. Miano, A. Mele, M. Silla, M. Bonano, P. Striano, R. Lanari, M. Di Ludovico, A. Prota, Space-borne DInSAR measurements exploitation for risk classification of bridge networks, J. Civ. Struct. Heal. Monit. (2024), https://doi.org/10.1007/s13349-024-00832-7.

[24] T.J. Wright, B.E. Parsons, Z. Lu, Toward mapping surface deformation in three dimensions using InSAR, Geophys. Res. Lett. 31 (2004), https://doi.org/10.1029/2003GL018827.

[25] S. Selvakumaran, C. Rossi, A. Marinoni, G. Webb, J. Bennetts, E. Barton, S. Plank, C. Middleton, Combined InSAR and terrestrial structural monitoring of bridges, IEEE Trans. Geosci. Remote Sens. 58 (2020) 7141–7153, https://doi.org/10.1109/TGRS.2020.2979961.

[26] M. Foumelis, Vector-based approach for combining ascending and descending persistent scatterers interferometric point measurements, Geocarto Int. 33 (2018) 38–52, https://doi.org/10.1080/10106049.2016.1222636.

[27] D.A. Talledo, A. Miano, M. Bonano, F. Di Carlo, R. Lanari, M. Manunta, A. Meda, A. Mele, A. Prota, A. Saetta, A. Stella, Satellite radar interferometry: potential and

limitations for structural assessment and monitoring, J. Build. Eng. 46 (2022) 103756, https://doi.org/10.1016/j.jobe.2021.103756.

[28] G. Bonaldo, A. Caprino, F. Lorenzoni, F. da Porto, Monitoring displacements and damage detection through satellite MT-InSAR techniques: a new methodology and application to a case study in Rome (Italy), Remote Sens. 15 (2023) 1177, https://doi.org/10.3390/rs15051177.

[29] D. Infante, D. Di Martire, P. Confuorto, S. Tessitore, R. Tòmas, D. Calcaterra, M. Ramondini, Assessment of building behavior in slow-moving landslide-affected areas through DInSAR data and structural analysis, Eng. Struct. 199 (2019) 109638, https://doi.org/10.1016/j.engstruct.2019.109638.

[30] V. Gagliardi, L.B. Ciampoli, F. D'Amico, F. Tosti, A.M. Alani, A. Benedetto, A novel geo-statistical approach for transport infrastructure network monitoring by Persistent Scatterer Interferometry (PSI), in: 2020 IEEE radar Conf, IEEE, 2020, pp. 1–6, https://doi.org/10.1109/RadarConf2043947.2020.9266336.

[31] L. Cascini, S. Ferlisi, G. Fornaro, R. Lanari, D. Peduto, G. Zeni, Subsidence monitoring in Sarno urban area via multi-temporal DInSAR technique, Int. J. Remote Sens. 27 (2006) 1709–1716, https://doi.org/10.1080/01431160500296024.

[32] G. Aslan, Z. Cakir, C. Lasserre, F. Renard, Investigating subsidence in the Bursa plain, Turkey, using ascending and descending Sentinel-1 satellite data, Remote Sens. 11 (2019) 85, https://doi.org/10.3390/rs11010085.

[33] A. Tamburini, M. Bianchi, C. Giannico, F. Novali, Retrieving surface deformation by PSInSAR™ technology: a powerful tool in reservoir monitoring, Int. J. Greenh. Gas Control. 4 (2010) 928–937, https://doi.org/10.1016/j.ijggc.2009.12.009.

[34] V. Tofani, F. Raspini, F. Catani, N. Casagli, Persistent Scatterer interferometry (PSI) technique for landslide characterization and monitoring, Remote Sens. 5 (2013) 1045–1065, https://doi.org/10.3390/rs5031045.

[35] P. Giordano, Z. Turksezer, M. Previtali, M. Limongelli, Damage detection on a historic iron bridge using satellite DInSAR data, Struct. Health Monit. 21 (2022) 2291–2311, https://doi.org/10.1177/14759217211054350.

[36] M. Costantini, F. Minati, F. Trillo, A. Ferretti, F. Novali, E. Passera, J. Dehls, Y. Larsen, P. Marinkovic, M. Eineder, R. Brcic, R. Siegmund, P. Kotzerke, M. Probeck, A. Kenyeres, S. Proietti, L. Solari, H.S. Andersen, European Ground Motion Service (EGMS), in: 2021 IEEE Int. Geosci. Remote Sens. Symp. IGARSS, IEEE, 2021, pp. 3293–3296, https://doi.org/10.1109/IGARSS47720.2021.9553562.

[37] E. Cosenza, D. Losanno, Assessment of existing reinforced-concrete bridges under road-traffic loads according to the new Italian guidelines, Struct. Concr. 22 (2021) 2868–2881, https://doi.org/10.1002/suco.202100147.

[38] E. Bassoli, L. Vincenzi, F. Grassi, F. Mancini, A multi-temporal DInSAR-based method for the assessment of the 3D rigid motion of buildings and corresponding uncertainties, J. Build. Eng. 73 (2023) 106738, https://doi.org/10.1016/j.jobe.2023.106738.

[39] K.M. Olsen, M.T. Calef, P.S. Agram, Contextual uncertainty assessments for InSAR-based deformation retrieval using an ensemble approach, Remote Sens. Environ. 287 (2023) 113456, https://doi.org/10.1016/j.rse.2023.113456.

[40] S. Zwieback, F.J. Meyer, Reliable InSAR phase history uncertainty estimates, IEEE Trans. Geosci. Remote Sens. 60 (2022) 1–9, https://doi.org/10.1109/TGRS.2022.3146816.

[41] W.D. Barnhart, R.B. Lohman, Characterizing and estimating noise in InSAR and InSAR time series with MODIS, geochemistry, Geophys. Geosystems. 14 (2013) 4121–4132, https://doi.org/10.1002/ggge.20258.

[42] ReLUIS, Linee guida per l'utilizzo dei dati interferometrici satellitari ai fini dell'interpretazione del comportamento strutturale delle costruzioni. https://www.reluis.it/it/divulgazione/archivio-news/anno-2023/270-linee-guida-per-l-utilizzo-dei-dati-interferometrici-satellitari-ai-fini-dell-interpretazione-del-comportamento-strutturale-delle-costruzioni.html, 2023.

[43] M. Manunta, C. De Luca, I. Zinno, F. Casu, M. Manzo, M. Bonano, A. Fusco, A. Pepe, G. Onorato, P. Berardino, P. De Martino, R. Lanari, The parallel SBAS approach for Sentinel-1 interferometric wide swath deformation time-series generation: algorithm description and products quality assessment, IEEE Trans. Geosci. Remote Sens. (2019), https://doi.org/10.1109/TGRS.2019.2904912.

[44] F. Casu, S. Elefante, P. Imperatore, I. Zinno, M. Manunta, C. De Luca, R. Lanari, SBAS-DInSAR parallel processing for deformation time-series computation, IEEE J. Sel. Top. Appl. Earth Obs. Remote Sens. (2014), https://doi.org/10.1109/JSTARS.2014.2322671.

[45] F. Raspini, F. Caleca, M. Del Soldato, D. Festa, P. Confuorto, S. Bianchini, Review of satellite radar interferometry for subsidence analysis, Earth-Science Rev. 235 (2022) 104239, https://doi.org/10.1016/j.earscirev.2022.104239.

[46] A. Moreira, P. Prats-Iraola, M. Younis, G. Krieger, I. Hajnsek, K.P. Papathanassiou, A tutorial on synthetic aperture radar, IEEE Geosci. Remote Sens. Mag. 1 (2013) 6–43, https://doi.org/10.1109/MGRS.2013.2248301.

[47] P.A. Rosen, S. Hensley, I.R. Joughin, F.K. Li, S.N. Madsen, E. Rodriguez, R. M. Goldstein, Synthetic aperture radar interferometry, Proc. IEEE 88 (2000) 333–382, https://doi.org/10.1109/5.838084.

[48] A.K. Gabriel, R.M. Goldstein, H.A. Zebker, Mapping small elevation changes over large areas: differential radar interferometry, J. Geophys. Res. 94 (1989) 9183, https://doi.org/10.1029/JB094iB07p09183.

[49] A. Ferretti, C. Prati, F. Rocca, Permanent scatterers in SAR interferometry, IEEE Trans. Geosci. Remote Sens. (2001), https://doi.org/10.1109/36.898661.

[50] M. Bonano, M. Manunta, A. Pepe, L. Paglia, R. Lanari, From previous C-band to new X-band SAR systems: assessment of the DInSAR mapping improvement for deformation time-series retrieval in urban areas, IEEE Trans. Geosci. Remote Sens. 51 (2013) 1973–1984, https://doi.org/10.1109/TGRS.2012.2232933.

[51] Iceye. https://www.iceye.com/satellites, 2025 [accessed 26 June 2025].

[52] Capella Space. https://www.capellaspace.com/, 2025 [accessed 26 June 2025].

[53] D. Tonelli, V.F. Caspani, A. Valentini, A. Rocca, R. Torboli, A. Vitti, D. Perissin, D. Zonta, Interpretation of bridge health monitoring data from satellite InSAR technology, Remote Sens. 15 (2023) 5242, https://doi.org/10.3390/rs15215242.

[54] Q. Huang, M. Crosetto, O. Monserrat, B. Crippa, Displacement monitoring and modelling of a high-speed railway bridge using C-band Sentinel-1 data, ISPRS J. Photogramm. Remote Sens. 128 (2017) 204–211, https://doi.org/10.1016/j.isprsjprs.2017.03.016.

[55] A. Vorwagner, M. Kwapisz, P. Leopold, M. Ralbovsky, K.H. Gutjahr, T. Moser, Verformungsmonitoring von Brücken mittels berührungsloser Satellitenradarmessungen, Beton- Und Stahlbetonbau. (2024), https://doi.org/10.1002/best.202400017.

[56] M.H. Faber, Statistics and Probability Theory, Springer Netherlands, Dordrecht, 2012, https://doi.org/10.1007/978-94-007-4056-3.

[57] M. Crosetto, O. Monserrat, M. Cuevas-González, N. Devanthéry, B. Crippa, Persistent Scatterer interferometry: a review, ISPRS J. Photogramm. Remote Sens. 115 (2016) 78–89, https://doi.org/10.1016/j.isprsjprs.2015.10.011.

[58] G. Sacheri, Il nuovo Ponte Palatino sul Tevere in Roma, L'ingegneria Civ. e Le Arti Ind. 18 (1892).

[59] P.F. Giordano, M. Previtali, M.P. Limongelli, Monitoring of a metal bridge using DInSAR data, in: P. Rizzo, A. Milazzo (Eds.), Eur. Work. Struct. Heal. Monit. EWSHM 2022. Lect, Notes Civ. Eng., Springer, Cham, 2023, pp. 397–406, https://doi.org/10.1007/978-3-031-07258-1_41.